Resource

Cell

Mapping the Fine-Scale Organization and Plasticity of the Brain Vasculature

Graphical Abstract

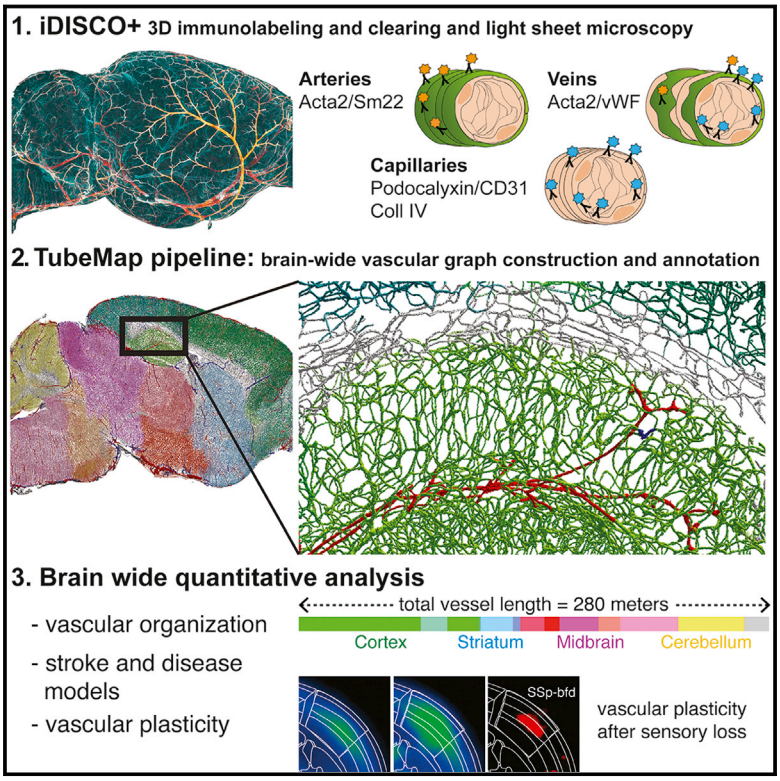

Highlights

- TubeMap enables fast construction of labeled vascular graphs from TB-sized images
- Automated arterio-venous annotations are based on iDISCO+ immunolabeling
- We measure regional variations in vessel topology and arterio-venous distances
- We study the plasticity of this network in stroke and sensory-deprivation models

Authors

Christoph Kirst, Sophie Skriabine, Alba Vieites-Prado, ..., Nicolas Michalski, Marc Tessier-Lavigne, Nicolas Renier

Correspondence

christoph.kirst@ucsf.edu (C.K.), nicolas.renier@icm-institute.org (N.R.)

In Brief

TubeMap, a pipeline for characterizing brain-wide variations in vascular topology, including vessel network structure, geometry, and arterio-venous labeling, was developed and used to investigate vascular remodeling in models of ischemic stroke and sensory loss.

Kirst et al., 2020, Cell *180*, 780–795
February 20, 2020
https://doi.org/10.1016/j.cell.2020.01.028

CellPress

Cell

Resource

Mapping the Fine-Scale Organization and Plasticity of the Brain Vasculature

Christoph Kirst,[1,2,3,7,*] Sophie Skriabine,[1,7] Alba Vieites-Prado,[1,7] Thomas Topilko,[1] Paul Bertin,[1] Gaspard Gerschenfeld,[4] Florine Verny,[1] Piotr Topilko,[4] Nicolas Michalski,[5] Marc Tessier-Lavigne,[6] and Nicolas Renier[1,8,*]

[1]Laboratoire de Plasticité Structurale, Sorbonne Université, ICM Institut du Cerveau et de la Moelle Epinière, INSERM U1127, CNRS UMR7225, 75013 Paris, France

[2]Center for Physics and Biology and Kavli Neural Systems Insittute, The Rockefeller University, 10065 New York, NY, USA

[3]Kavli Institute for Fundamental Neuroscience and Anatomy Department, Sandler Neuroscience Building, Suite 514G, 675 Nelson Rising Lane, University of California, San Francisco, San Francisco, CA 94158, USA

[4]Institut Mondor de Recherche Biomédicale, INSERM U955-Team 9, Créteil, France

[5]Unité de Génétique et Physiologie de l'Audition, UMRS 1120, Institut Pasteur, INSERM, 75015 Paris, France

[6]Department of Biology, Stanford University, Stanford, CA 94305, USA

[7]These authors contributed equally

[8]Lead Contact

*Correspondence: christoph.kirst@ucsf.edu (C.K.), nicolas.renier@icm-institute.org (N.R.)

https://doi.org/10.1016/j.cell.2020.01.028

SUMMARY

The cerebral vasculature is a dense network of arteries, capillaries, and veins. Quantifying variations of the vascular organization across individuals, brain regions, or disease models is challenging. We used immunolabeling and tissue clearing to image the vascular network of adult mouse brains and developed a pipeline to segment terabyte-sized multichannel images from light sheet microscopy, enabling the construction, analysis, and visualization of vascular graphs composed of over 100 million vessel segments. We generated datasets from over 20 mouse brains, with labeled arteries, veins, and capillaries according to their anatomical regions. We characterized the organization of the vascular network across brain regions, highlighting local adaptations and functional correlates. We propose a classification of cortical regions based on the vascular topology. Finally, we analysed brain-wide rearrangements of the vasculature in animal models of congenital deafness and ischemic stroke, revealing that vascular plasticity and remodeling adopt diverging rules in different models.

INTRODUCTION

Blood flows within the brain through an intricate vascular network of arteries, capillaries, and veins. The high metabolic needs of the brain and its low capacity to store energy require that neuronal and vascular functions are intimately linked (Girouard and Iadecola, 2006). Minimal perturbations of the blood flow impact neuronal function and can compromise neuron survival (Zlokovic, 2008). Conversely, neuronal activity modulates hemodynamics (Ances, 2004). Thus, many neurological disorders have a vascular component, and most vascular alterations have consequences on brain functions (Iadecola, 2013; Kisler et al., 2017; Zlokovic, 2011).

The cerebral vasculature is challenging to study as it spans several spatial scales (from micron-sized capillaries tiling the brain to vessels extending over several millimeters) and forms a highly complex network (Begley and Brightman, 2003) in which exchanges with the brain are tightly controlled by the blood-brain barrier (Zlokovic, 2008). 2-photon microscopy combined with cranial windows has been an essential tool to study the dynamics of blood flow and metabolism *in vivo* (Mächler et al., 2016; Roche et al., 2019). However, the impact of the vascular topology on the function of neural circuits is often overlooked because of the difficulty to extract information on the brain-wide vascular organization. Addressing these questions requires systematic comparisons of the fine structure of the vasculature in large volumes.

A comprehensive description of the organization and remodeling of the vasculature also calls for methods allowing the identification of the arterial, capillary, and venous components. Large-scale cerebral vascular reconstructions have been carried out to this day predominantly with dye filling strategies, in which a vessel-filling solution is perfused intracardially (Blinder et al., 2013; Kleinfeld et al., 2011; Quintana et al., 2019; Tsai et al., 2009). More recently, such injections have been combined with light sheet microscopy in optically cleared samples for large-scale reconstructions (Breckwoldt et al., 2016; Di Giovanna et al., 2018; Lagerweij et al., 2017; Liebmann et al., 2016; Lugo-Hernandez et al., 2017; Todorov et al., 2019; Zhang et al., 2018). While vessel-filling allows for a bright labeling that facilitates imaging and downstream analysis, the nature of the reconstructed vessels is unknown, and can, to this day, only be retrieved manually on highly resolved datasets (Blinder et al., 2013). Additionally, reproducibility is challenging with intracardiac perfusions (Quintana et al., 2019). Alternative labeling methods have been used, such as tail-vein lectin injections (d'Esposito et al., 2018), or the use of mouse genetic lines with labeled vessel walls (Jing et al., 2018). However, because these labels are faint, discontinuous, and leave the vessel centers

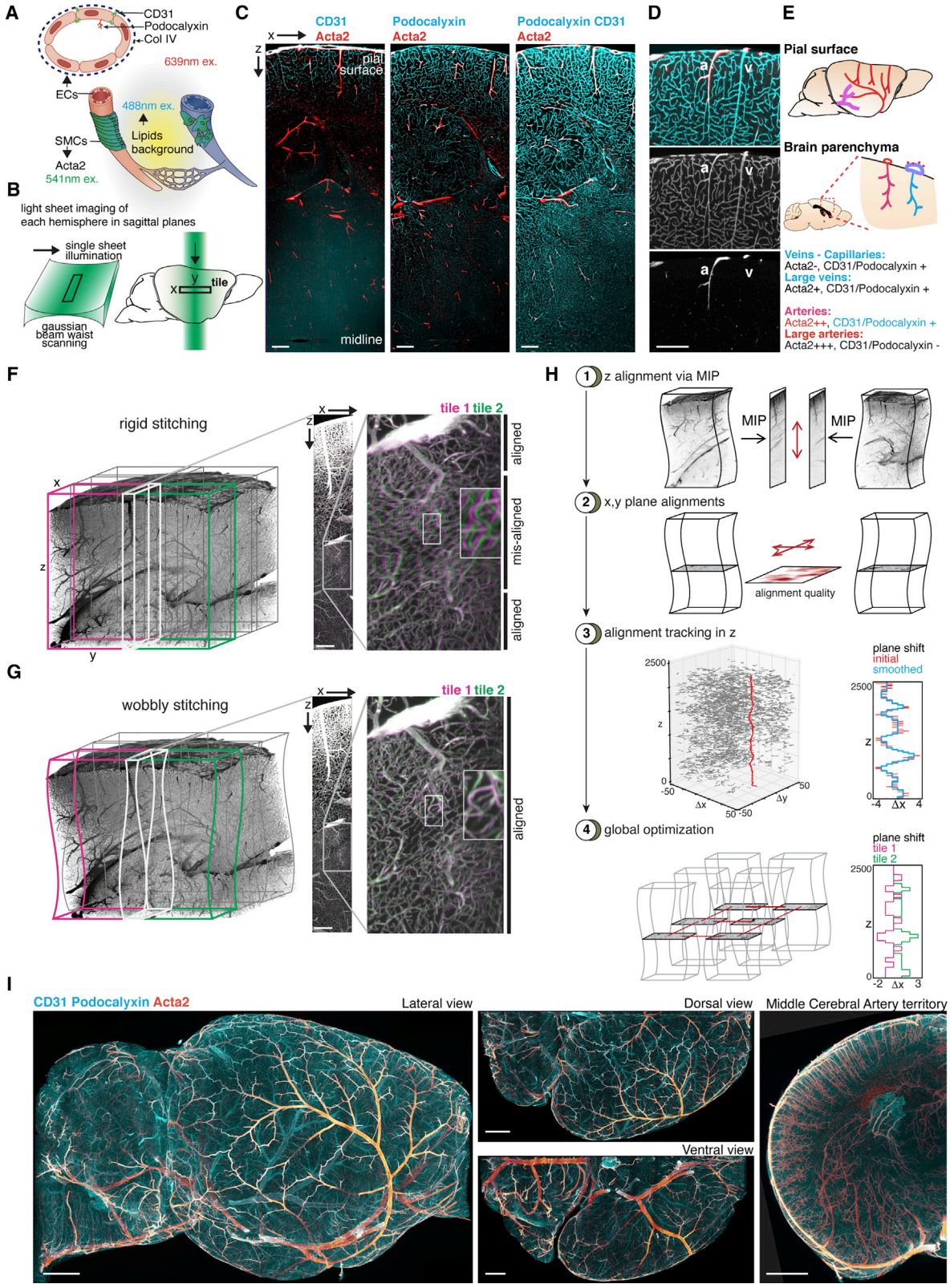

Figure 1. Deep Immunolabeling and Imaging of the Vasculature with Light Sheet Microscopy

(A–E) Complementary immunolabeling against CD31, podocalyxin, and Acta2 enables deep immunolabeling of the vasculature in intact perfused brains. (A) Immunolabeling strategy.

(legend continued on next page)

unlabeled, they pose an unsolved challenge for image processing at high resolution and large scales.

We explored the possibility of using immunolabeling and tissue-clearing to construct graphs of vascular networks. This strategy, in principle, offers several advantages. The structural labeling of vessel walls does not require intracardiac perfusion and would therefore allow the labeling of organs or embryos that are difficult or impossible to perfuse. Moreover, immunolabeling would enable the combination of a generic vessel signal with markers specific for each vessel type. So far, it has been difficult to balance labeling specificity versus epitope density using immunolabeling against the vessel walls in intact adult organs. In addition, there is also a lack of tools designed to process data from 3D fluorescent microscopy on terabyte-sized image stacks. Light sheet imaging and tiling artifacts lead to frequent duplication or fusions of vessels that greatly alter network topologies and compromise large-scale statistical comparisons of vascular datasets.

Here, we report a method to generate labeled (arteries, capillaries, and veins) and region-annotated vascular graphs of the mouse brain. It relies on an immunolabeling cocktail that produces a bright labeling of the vascular endothelial and smooth muscle cells in unsectioned brains using the iDISCO+ technique (Renier et al., 2016). To construct vascular graphs, we designed a complete processing pipeline, TubeMap, which addresses issues of vessel duplication and other imaging artifacts as well as the multi-scale nature and hollow tube structure of the vasculature network. TubeMap is optimized to work on large terabyte datasets and integrates functions to handle, visualize, and analyze the reconstructed vascular networks made of several millions of vessels.

Using this novel pipeline, we measured the regional variations of the mouse cerebral vascular topology. We found that while the density of the capillaries can vary up to an order of magnitude between regions, their distance to the nearest arterial or venous endpoints are similar throughout the brain. We used clustering methods to compare the organization of neocortical regions. Finally, we analyzed the remodeling of the vascular network in two different pathological conditions: congenital sensory deprivation of the auditory system and brain ischemia in adult animals. These models showed two distinct modes of vascular remodeling and plasticity, with cross-modal long-range changes of the vascular density in congenitally deaf mice and region-independent reorientation of capillaries in stroked brains.

RESULTS

Labeling and Imaging of the Vasculature

Complete labeling of the brain endothelial cells with antibodies is challenging, due to the density of epitopes. We verified that the iDISCO+ processing time and pre-treatments did not affect the integrity of the vasculature (Figure S1A). To enhance the signal of the vessels immunolabeling, we sought to design a ''super-polyclonal'' immunoglobulin cocktail and tested a panel of antibodies targeting proteins broadly expressed by endothelial cells: CD31 (Newman et al., 1990), collagen IV, and podocalyxin (Horvat et al., 1986; Testa et al., 2009) (Figure 1A). None of the anti-CD31 antibodies tested yielded sufficient signal. Anti-podocalyxin labeling improved the signal deep in the brain, but still with a low signal-to-noise ratio at the center when used on its own (Figures 1C and S1B). However, combining both markers labeled the vasculature with high signal-to-noise ratios throughout the brain (Figure 1C). To increase the flexibility of the method, we tested different host combinations of these markers (Figures S1B–S1D; Methods S1). We verified that the complete vasculature was labeled with this strategy, by staining for CD31 on sections after an anti-podocalyxin whole-mount labeling (Figure S1E).

We complemented this labeling with additional markers specific to arteries. We explored the use of smooth muscle actin (Acta2) and transgelin (Sm22), both known to have high expression levels within arterial walls and weaker in veins (Brunet et al., 2014; Hill et al., 2015; Vanlandewijck et al., 2018). iDISCO+ labeling of Acta2 and Sm22 yielded, as expected, a dense arterial signal, while surface and large penetrating veins had a weak and patchy distribution (Figure S2A; Video S1). Validation of the volume Acta2 labeling on sections confirmed that all arteries were labeled but smaller, higher order branches were occasionally only visible from the section staining (Figure S2B). We finally tested the possibility to discriminate veins by screening for venous-enriched markers (Vanlandewijck et al., 2018) and found that von Willebrand factor (vWF) immunolabeling was compatible with volume staining and enabled veins/arteries discrimination on raw data (Figure S2C).

Vascular imaging requires high resolutions, and we strived to find a compromise between resolution, data handling, and acquisition speed using a commercial light sheet microscope. To maximize the z resolution, we optimized the sheet curvature and tiling layout (Figure 1B). The apparent diameters of

(B) Light sheet scanning strategy along the narrow waist to accelerate acquisitions and maximize the optical resolution.
(C) Whole brain immunolabeling of the vasculature with iDISCO+ for CD31 and podocalyxin (blue) and Acta2 (red), imaged with light sheet microscopy. Transverse cortical 50-μm thick projection plane from a central tile.
(D) Acta2 enables the discrimination of arteries in the brain parenchyma: an Acta2+ artery is visible (a), and a nearby Acta2- vein (v).
(E) Summary of the signal distribution in the brain.
(F) Light sheet scans produce non-stitchable columns. A projection along the overlapping region of the tile is shown with misalignments noticeable in a few planes at the center of the inset.
(G) WobblyStitcher addresses recurrent stitching issues to produce seamless datasets. The same alignment is shown after non-rigid alignment of the planes, correcting the vessel duplications.
(H) Presentation of the stitching pipeline: (1) tile pairs are first aligned in z; (2) each plane is aligned individually along x,y; (3) tracking of the alignment quality for a smooth correction of the rigid stitching artifacts and smoothing of the resulting trajectories; (4) global optimization of all plane positions.
(I) Raw data resulting from the labeling, imaging, and stitching strategy, shown in ventral, dorsal, and lateral orientations. A thick projection of part of the middle cerebral artery territory is shown on the right, with striatal penetrating arteries visible.
Scale bars represent 300 μm in (C), (D), (F), and (G) and 1 mm in (I).

capillaries on raw data were between 2.6 and 2.7 px in x or y (about 4.2 μm) and between 4.0 px in z at the center of the tile to 5.8 px at the level of the blended tiles overlap, the less resolved portions of the data (Figures S3A–S3C).

Stitching the mosaic accurately is necessary to prevent capillary duplications. Commonly used stitchers, such as Terastitcher (Bria and Iannello, 2012) or Imaris Stitcher produced many tiling errors on our data (about 10% of the borders where misplaced) (Figures S4A and S4B). Although BigStitcher (Hörl et al., 2019) improved on tile placement, we noticed that mechanical jitters of stage movements still prevented accurate alignments throughout the stacks (Figure 1F). To solve these problems, we developed WobblyStitcher, a tool for robust and non-rigid stitching of terabyte datasets (Figures 1G and 1H) (see STAR Methods for details on the stitcher and computing resources). WobblyStitcher produced accurate non-rigid placement of the data and was robust in placing challenging planes at the edge of the sample, virtually eliminating object duplications in the dataset and producing continuous images of vessels (Figures 1I, S4C, and S4D).

Vasculature Graph Construction

Despite a high signal-to-noise ratio (Figure S3A), we found that a processing pipeline based on a single filter could not accurately segment vessels in our data due to glow and shadows artifacts, but also because of the widely varying sizes and signal intensities of vessels. To tackle the multi-scale nature of our data, we implemented a collection of filters arranged in parallel paths (“multi-paths”) designed to process complex fluorescent microscopy images of very large sizes (TB) in a few hours on a standalone workstation (Figures 2A and 2B). Light-sheet imaging artifacts of streaking shadows that resemble vessels are first removed with 2 crossed 3D rank filters (Figure 2C). In a second step, the multi-path pipeline is used to binarize the vessels. Each path captures and handles different aspects of the vessel signal (Figures 2D–2G).

This first part of the pipeline can binarize different types of vascular datasets generated from gel filling or wall labeling methods. However, the labeling of endothelial and arterial walls produces images of both solid (capillaries) and hollow tubes (veins and arteries). The segmentation of hollow vessels has not been attempted yet on very large data (Bates et al., 2019). We used a machine-learning approach and designed a deep convolutional neural network (CNN) based on an architecture optimized for vessel segmentation on large 3D datasets to fill empty vessels (Livne et al., 2019). Our CNN was trained using whole-brain datasets containing only filled vessels and imaged using the binarization pipeline (Figures 2H, S5A, and S5B; STAR Methods). Tested on an artificial dataset made from a real graph of vessels with radii ranging from 2 to 25 pixels (Figures S5C and S5D), the network had a false positive rate of 0.1% ± 0.06% pixels. We applied this CNN to both the vessels and arterial binary masks to obtain filled tubes throughout the datasets (Figures 2H, S5E, and S5F).

The binary image is then used to construct the graph of the vasculature network (Figure 2I). We built a highly optimized 3D skeletonization algorithm based on a directional parallel thinning method and discrete topology (Figure 2I). Our skeletonization step traces the center lines of vessels in a typical dataset of 10 billion foreground pixels in about 1 h.

Graphs were then created from the centerline image and augmented by information about vessel geometry, identity, and brain annotation (Figures 2I and S6; STAR Methods). To determine vessels identity, seed points were placed on clearly identified large veins, based on their radii and low Acta2 expression. For arteries, seed points were placed on vessels with high Acta2 expression. Finally, the labels were expanded by tracing from these seed points down to capillary radii (Figures S6B–S6E).

To validate our pipeline (Figure 3A), we performed manual segmentation from the raw data in random cubes extracted from 3 locations in a whole brain scan, representative of the data heterogeneity (Figure S5G). After the manual segmentation, the whole scan was processed with TubeMap and the graph constructed. We found that 4.0% ± 1.7% of manually annotated vessel branches were missed by TubeMap, and 2.9% ± 1.8% of the branches present in the TubeMap graph had not been manually annotated.

Analysis of Vascular Graphs

We first constructed vascular graphs of brains from three perfused C57Bl6 3-month-old mice labeled for podocalyxin, CD31, and Acta2. We plotted 3D renders of these graphs to verify the consistency of our unsupervised reconstructions from identifiable hallmarks of the rodent’s cerebrovasculature (Figures 3B–3F). In the cortex, alternating penetrating arteries and veins as well as the laminar heterogeneity of capillary density were clearly visible, with higher densities of vessels in the isocortex than in the allocortex (Figure 3B) (Michaloudi et al., 2005; Schmid et al., 2019). Known laminar or radial patterns of capillary densities were visible in the hippocampus (Figure 3B), brainstem, midbrain (Figure 3D), or cerebellum (Figure 3E). We verified the quality of the vessel identity labeling from the expected organization of veins and arteries in the hippocampus, cerebellum, and spinal cord (Figure S7). In the hippocampus, alternating arcs of veins and arteries were observed (Figure 3C). In the cerebellum, arteries were detected primarily at the pial surface of the lobules and veins mostly in the white matter (Figure 3E). In the spinal cord, arteries where visible as arbors fanned out from the anterior and the posterior lateral spinal arteries (Figure S7B; Video S2). Vessels belonging to white matter tracts (Figure 3F, in white) were longer and less dense than their gray matter counterpart.

We then turned to a brain-wide quantitative analysis of the vascular network. The total length of the vasculature added up to 144 ± 2 m per hemisphere (n = 3). Using the Allen Brain Atlas annotation, we further resolved the vessel length density across different brain areas (Figure 4A) with the cortex contributing the largest part. Vessel length density varied widely at a sub-region level: for example, all cortical areas showed repetitive variations in the vessel length density across cortical layers (Figure 4A, inset).

We then included topological aspects into our analysis. We identified all branch points at which vessels split or join. A typical graph consisted of 3.2 million branch points and 4.4 million vessel segments per hemisphere. The brain-wide mean vessel branch point density was 6,400 per cubic millimeter (Figure 4B). However, many brain regions deviate by a wide margin

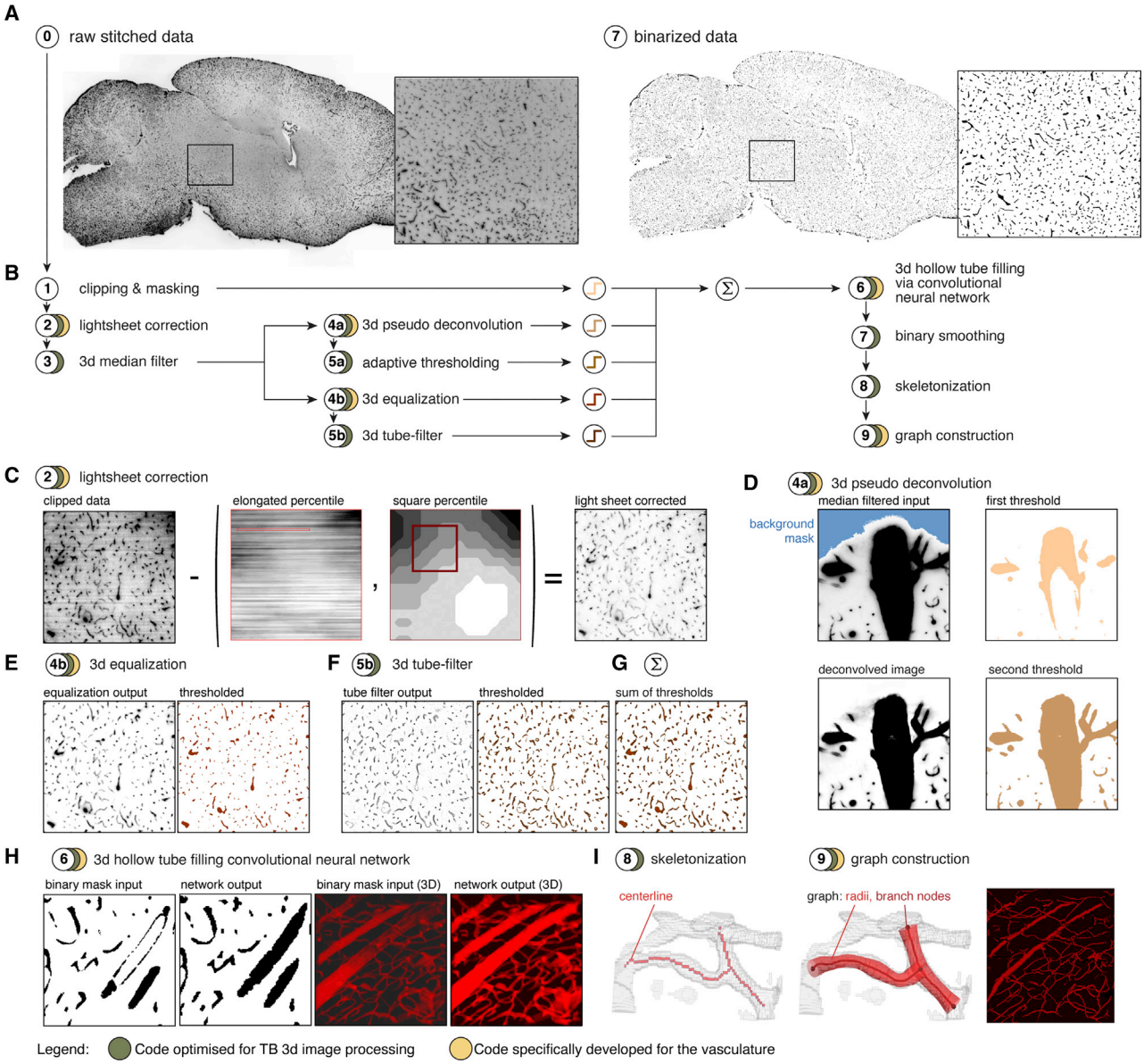

Figure 2. Vasculature Segmentation through Multi-path Binarization, Tube Filling, and Parallel Skeletonization

(A) Presentation of the image-processing pipeline for the binarization of vascular immunolabeling. Original data are on the left, and the binarization result is on the right.

(B) The multi-path TubeMap binarization is adaptable to segment complex immunolabeling signals and contains steps optimized for large 3D datasets (green circles) and steps specifically designed for the vasculature (yellow circles).

(C) A novel strategy for fast removal of light sheet striping artifact using a combination of 3D-rank filters. The input shows stripe artifacts (left). A local percentile filter with elongated structural element (red box) estimates the light sheet artifact at each voxel (middle left). To avoid removing vessels in that orientation it is compared to an estimate of the overall vessel intensity using a cubic structural element (brown box, middle right). The result is subtracted to give the corrected image (right).

(D) Pseudo deconvolution method to correct for shadows diffusing the edge of large vessels (top left). High threshold pixels are determined (top right) and a blurred version subtracted from the original image to give a pseudo-deconvolved image (bottom left), the thresholded version (bottom right) separates the large bright branches.

(E) Result of the 3D equalization (left) of the light sheet corrected image in (C). The vessel intensities are homogenized.

(F) Result of the Hessian tube filtering to enhance smaller and weaker vessels.

(G) Sum of the different multi-path filters.

(H) Convolutional neural network applied to the binary mask containing hollow vessels: a single plane is presented, the 3D projection of the region, and the resulting graph. The network fills empty tubes recognized from the binary mask.

(I) Fast centerline extraction via parallel thinning.. The centerline and binarized vasculature are then used to build a graph of the vasculature network and the geometry of the vessels.

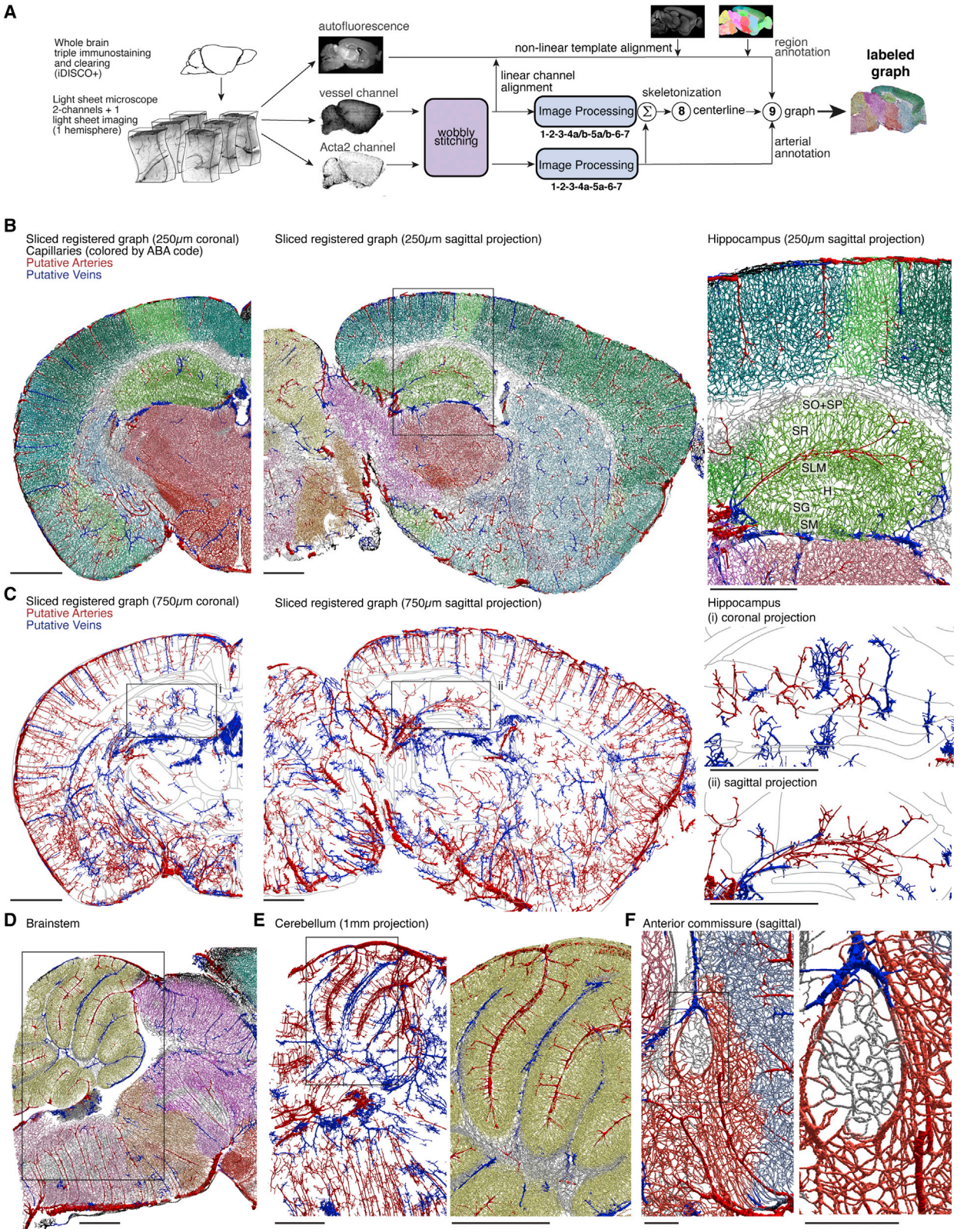

(legend on next page)

from this mean. The cortex, hippocampus, and striatum had densities below average in most regions with notable exceptions, for instance in the layer 4 of primary sensory regions. The densest nucleus of the brain was the median mammillary (Figures 4A and 4B; Table S1). Other notable nuclei known for their high densities are seen among sensory relays or neurosecretory regions and are indicated in Figures 4B and 4C.

Notably, the branch point density closely followed the vessel length density (Figures 4A versus 4B). Indeed, the number of vessel segments strongly correlated with the number of branch points in different brain regions with a ratio of 1.78 between them on average ($r^2 = 0.94$) (Figure 4C). If the vasculature network was a perfect tree in which each vessel would split into two vessels at each branch point (or conversely two vessels would join into one), this ratio would be expected to be precisely 3/2. The measured ratio is larger, indicating a level of redundancy in the vasculature network due the presence of either higher order branch points or loops. We therefore looked at the distribution of 4-points motifs across the brain to search for loops and found that although 85% of the network is made of simple forks, the remaining 15% contain loops indicative of the redundancy of the capillary bed (Figure 4E).

These results confirm that the capillary density of is highly heterogeneous throughout the brain (Craigie, 1945; Michaloudi et al., 2005; Schmid et al., 2019). Variations in capillary density are not correlated with neuronal density but could be related to oxidative metabolism at synapses (Keller et al., 2011). Apart from neurosecretory or homeostat-regulating nuclei, high capillary densities could denote higher levels of oxidative metabolism in synaptic terminals-rich regions that require high concentrations of ATP (Ashrafi and Ryan, 2017), as in sensory pathways.

As vessel length and vessel radius determine the resistance for a fluid to pass through a tube, we further measured length and radii of the vessel segments between two branch points. The length distribution in the cortex peaks at 20 μm, in agreement with previous studies (Blinder et al., 2013). However, the cortical distribution had longer vessel segments than other regions (Figure 4F). The joint distribution of length and radii across brain regions was comparable with previous studies in the cortex (Blinder et al., 2013), but again their distributions are slightly different in the other brain areas (Figure 4G).

We then included the arterial and venous annotations into our analysis. We asked whether the spatial variations of branch point and length densities across the brain affect the distances of capillaries to the next artery and vein. For this, we measured the length and the number of branch points along the shortest path from each vessel to the nearest artery or vein (Figure 4H). Interestingly, on average, the distance, as well as the branch order to the next vein, is larger than to the closest artery, suggesting that the distribution of blood requires a finer control than the collection (Figures 4I–4K). On average, a capillary is 5 or 7 branch points away from an artery or a vein, respectively (Figure 4I), and the mean shortest path between an artery and a vein that passes through a given vessel segment is 120 μm long (Figure 4J). We then focused on the distribution of arterial domains in the cortex. We isolated individual cortical arteries (Figure 4L) and estimated their capillary domain based on the previously calculated shortest distances (Figure 4M). We then counted the vessels in each arterial domain. The distribution of domain sizes peaked between 200 to 1,000 vessels per domain, but very large domains made of over 5,000 vessels were also found (see example in Figure 4M).

We finally chose to investigate in more detail the regional variations in the organization of the isocortex by extracting and comparing a selected set of features: we first extracted branch point densities in each layer, which were higher in the sensory cortices, especially in layer 4 (Figure 5A). We also extracted the position of arterial branches and end points (Figure 5B). Next, we measured the orientation of vessel branches, by considering the vector between two branching vertices and determined whether it was predominantly planar or radially oriented. We noticed that in all sensory regions, the upper layers had higher proportions of radially oriented vessels (Figure 5C). Conversely, integrative and motor regions had an equal mix of radial and planar oriented vessels between upper and deeper layers (Figures 5C and 5D). To combine the data from all the extracted features, we measured the differences between the distribution of these features across layers averaged from 3 brains. This separated two groups of regions: a block of sensory areas and another of integrative/motor areas (Figures 5D and 5E). This finding suggests that the type of computation performed across cortical layers strongly influences the organization of the vascular topology in the cortex.

Mapping Vascular Network Plasticity

The brain vasculature is a plastic network that can incur large-scale rearrangements following various types of insults, such as

Figure 3. Unsupervised Construction of Labeled Vascular Datasets

(A) The full TubeMap pipeline.

(B–F) Slices through a vascular brain graph, obtained from a C57bl6 3-month-old female mouse, plotted with ClearMap 2.0. Arteries are indicated in red, putative veins in blue, and capillaries are colored according to their regional annotation.

(B) 250-μm coronal and sagittal slices of the graph, showing the general organization of the cerebral vasculature and its regional variations. The inset shows a detail at the level of the hippocampus, with an arterial arc visible.

(C) 750-μm coronal and sagittal slices taken at the same levels, showing only labeled veins and arteries. Insets show sagittal and coronal views of the hippocampus, showing alternating arterial and venous arcs.

(D) 250-μm projection at the level of the brainstem midline, showing the radial organization of veins and arteries in the hindbrain and superior colliculus.

(E) Detail of a 1-mm midline sagittal slice at the level of the cerebellum: veins are predominantly located in the white matter and arteries at the pial surface of the lobules.

(F) Detail of the anterior commissure at a midline level (sagittal section). The white annotated vessels (fiber tracts) are longer and less dense that the gray matter vessels (red, thalamus; light blue, striatum).

Abbreviations: SO, stratum oriens, SP, stratum pyramidale, SLM, stratum lacunosum moleculare, SM, stratum moleculare, SG, stratum granulosum, H,: hylus. Scale bars represent 1 mm, except in (F) (250 μm).

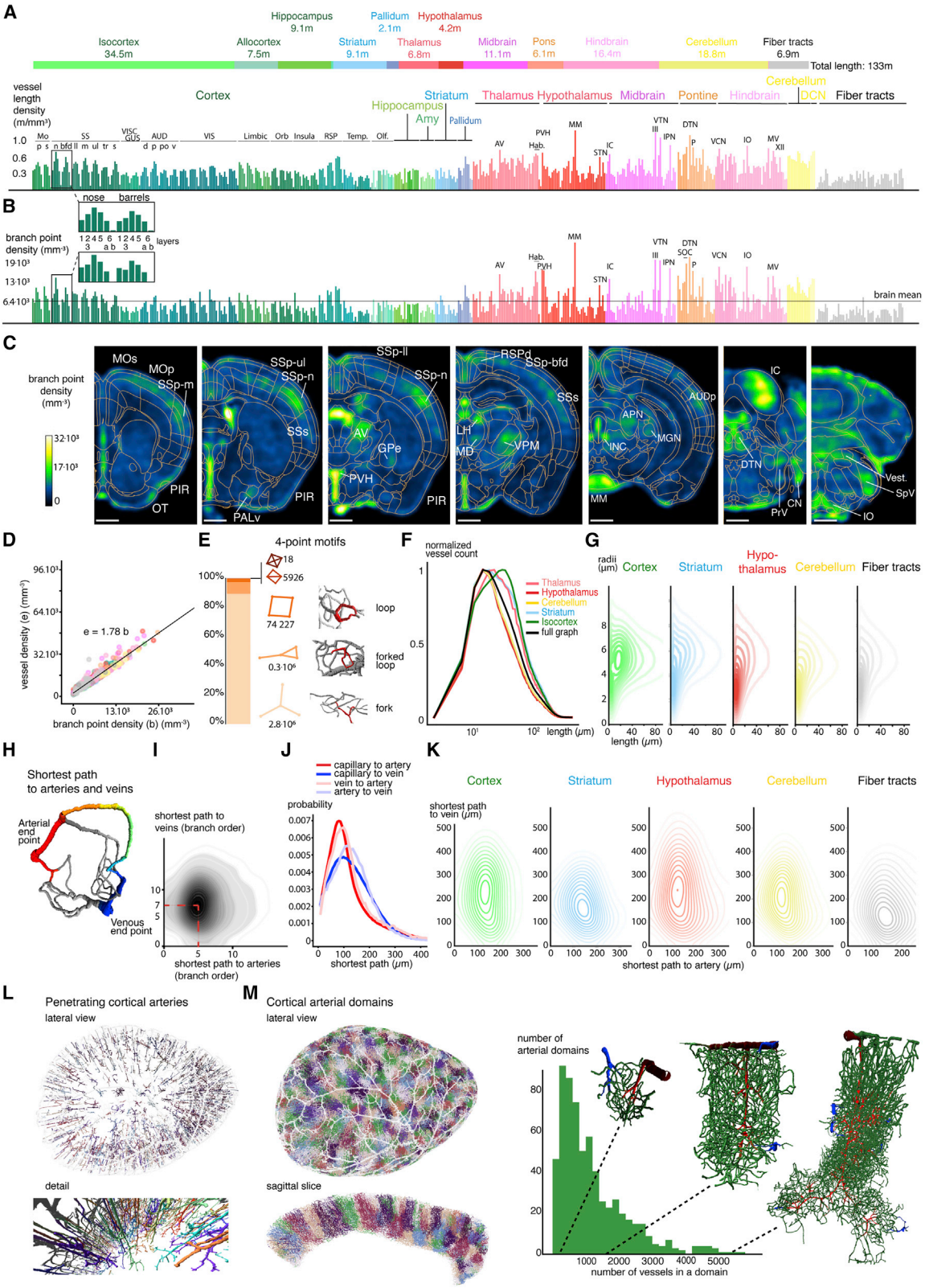

(legend on next page)

traumatic brain injury (Cao et al., 2015; Gama Sosa et al., 2019), stroke (Liu et al., 2014), or epilepsy (Arango-Lievano et al., 2018). It can also be remodeled by changes in neuronal activity levels, albeit mostly during embryonic and early post-natal development (Harb et al., 2013; Lacoste et al., 2014; Whiteus et al., 2014). However, the extent of these changes at the whole brain scale is unclear because the focus has so far been either on the capillary network in a small region (Harb et al., 2013) or on arterial network in a large region (Lu et al., 2012).

As a model of adult plasticity, we examined the nature of long-term changes to the vascular network 3 weeks after an ischemic stroke provoked by electrocauterization of the middle cerebral artery, a procedure that creates a focal ischemia in the dorso-lateral cortex. To avoid damaging potentially fragile vessels, we prepared drop-fixed brains from control and stroked animals, which we stained for podocalyxin, Acta2, and mouse immunoglobulins (as in Figures S5A and S5B). We first examined the middle cerebral artery (Figure 6A). The branch connecting the ventral circle of Willis to the dorsal arbor was missing (a stub of the branch is still visible ventrally), while the arterial dorsal arbor originating from the former degraded branch was preserved, hinting to the maintenance of the dorsal perfusion routes. When compared the vascular graphs of 3 control and 3 infarcted animals (Figures 6B and 6C; Video S3). The center of ischemia in the supplemental somatosensory cortex (SSs, 2 brains) or in the nearby mouth somatosensory cortex (SSp-m, 1 brain) was noticeable from the scans due to a higher tissue autofluorescence and the presence of cellular debris. The capillary branch point densities outside of the ischemic area was not significantly different from the controls when averaged as voxelized densities (Figures 6B, 6C, and 6E). However, a closer inspection of the center of ischemia and its surrounding volume revealed a striking reorganization of the capillaries so they were more oriented toward the ischemic center (Figure 6D). Orientation color-coding of the vessels from the graph highlighted the reduction in radial orientations (in green) in proportion to the vessels oriented along the cortical plane (in blue/red, Figure 6D). Following this observation, we quantified the vessel orientations between groups by voxelizing accumulated orientations. Accumulated orientations were different in the cortical regions of the stroked group around the ischemic center with a loss of the radial component (Figure 6F). The vessel orientation remodeling extended across several cortical regions, but didn't propagate to subcortical regions. This result suggests that density-preserving remodeling of vessel orientations is a strong factor in adult vascular plasticity in a model of induced ischemia.

The vascular topology can adapt to changes in neuronal activity levels early in life (Harb et al., 2013; Lacoste et al., 2014; Whiteus et al., 2014). Long-range effects of a loss in specific sensory inputs on the organization of the vasculature in unrelated brain regions have not been studied yet. Because we previously noticed that the auditory system has higher densities of branching vessels than neighboring regions at most relays (Figures 4A and 4B), we compared the vasculature of congenitally deaf mice to the one of control mice of the same background (FVB). Otoferlin (otof), defective in a recessive form of profound congenital deafness (Roux et al., 2006; Yasunaga et al., 1999) acts as a calcium sensor for synaptic vesicle release at the first relay synapse of the auditory pathways (Michalski et al., 2017). In *Otof*$^{-/-}$ mice, sound-evoked neuronal activity is absent but spontaneous activity during embryonic development is undisturbed, so that the initial neuronal projections still develop normally (Müller et al., 2019).

We generated graphs from 3 control and 3 *Otof*$^{-/-}$ mice 2 months of age. We did not observe a change in the number of penetrating arteries in the primary auditory cortex (Figure 7A), as previously reported (Adams et al., 2018). We compared then the branch densities of all vessels from averaged registered voxel maps obtained. There was a significant ($p < 0.01$), though small, reduction of branch point density in the *Otof*$^{-/-}$ auditory cortex as assessed from the voxel map. Strikingly, the p value map revealed an increase in branch densities in the somatosensory barrel cortex (Figure 7B), as well as in the visual cortex, suggesting a cross-modal compensation for the loss of auditory input. Intriguingly, a few integrative regions, such as the peri- and ectorhinal areas, strongly connected to sensory cortices also showed a significant increase in branch point densities in the deaf *Otof*$^{-/-}$ mice.

Figure 4. Properties of the Whole Brain Vascular Graph

(A) Added vessel lengths in meters across major brain regions in 1 hemisphere (top, example of 1 brain), and average length density across all brain regions in meters per cubic mm (bottom, n = 3). The distribution of lengths densities is highly variable across brain regions. A detail of cortical layers is shown as an inset.
(B) Branch-point density across brain regions, showing similar trends as in (A).
(C) Spatial visualization of the distribution of branch point densities across the brain revealing hotspots of high vascular density related to specific nuclei.
(D) Vessel density versus branch point density are highly correlated across brain regions ($r^2 = 0.94$). The proportion of vessels to branch points of 1.78 indicates a systematic redundancy in the network.
(E) Counts of 4-point motifs in the vasculature graph throughout the brain. Although the fork motif dominates, motifs with local cycles constitute ~15% of the network.
(F) Distribution of vessel branch lengths in major brain regions.
(G) Joint distributions of branch length and radius across brain regions.
(H) Example of a shortest path (in color) between an artery (red) and a vein (blue) with other possible paths (in gray).
(I) Number of branches from all capillaries to their nearest artery or vein.
(J) Length of the shortest paths from each capillary branch to the nearest artery (red) or vein (blue) and from arterial vessels to the nearest vein (light blue) and venous vessels to the closest artery (light red).
(K) Joint distribution of the shortest path lengths from each capillary to their nearest artery and vein for major brain regions.
(L) Roots of individual penetrating arteries isolated in the cortex.
(M) Distribution of the sizes of arterial domains defined by shortest distance to the arterial roots in the cortex. Examples of small, medium-sized, and large domains are shown.
Scale bars represent 1 mm.

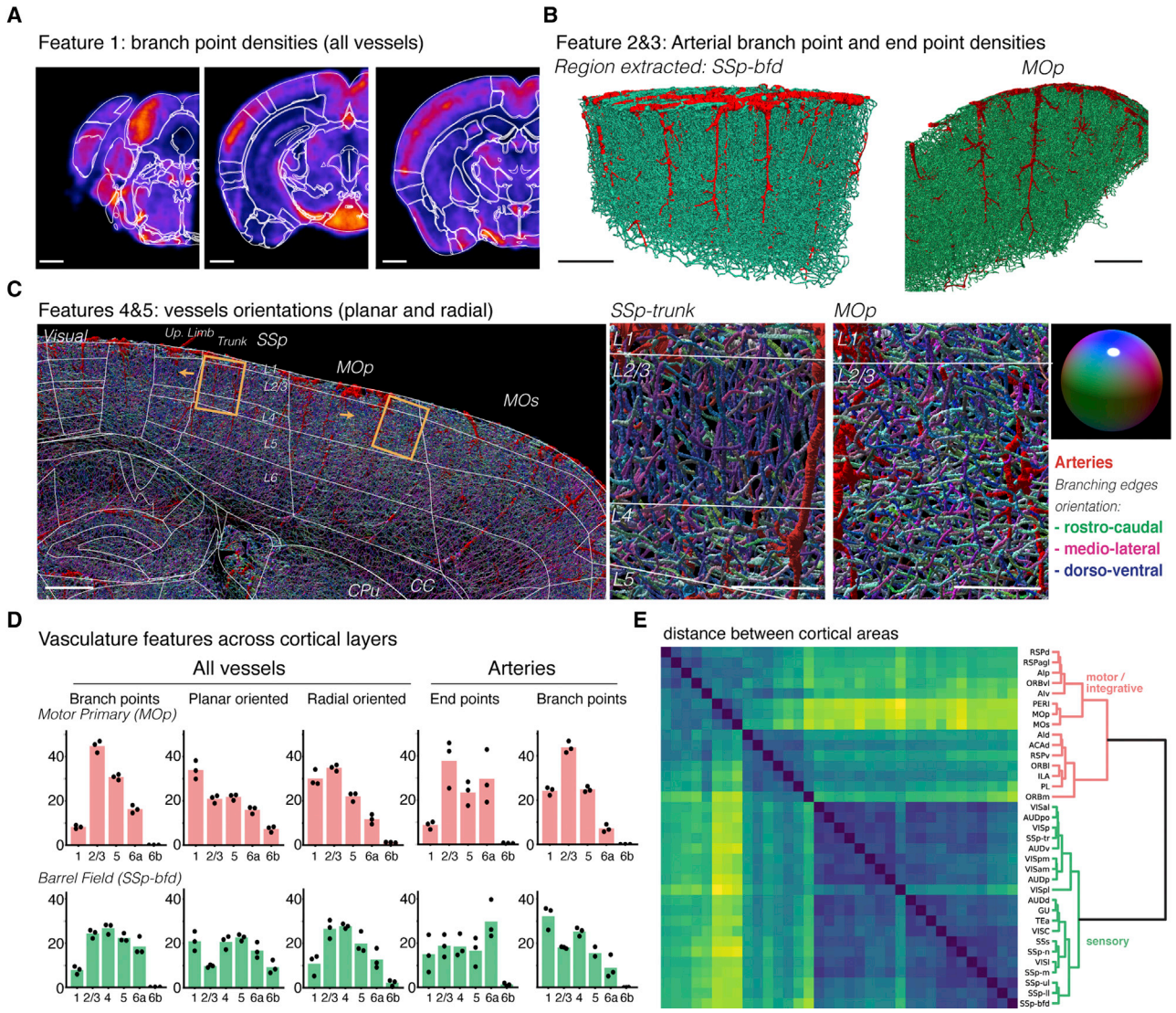

Figure 5. Regional Specificity of the Layered Structure of the Cortical Vasculature

(A–C) Features extraction of the vasculature from cortical regions. (A) Branch point density. Higher densities are seen in the sensory cortices, in particular in layers 4. (B) Arterial branch points with two representative regions are shown: barrels (SSp-bfd) and primary motor (MOp). (C) Color-coded branch orientations show layering in the somatosensory and motor cortices. The vessels in the somatosensory cortex have predominant radial orientations in upper layers 2/3 (blue), while the motor cortex has a mix of tangential (green-pink) and radial orientations across all layers.

(D) Distribution of features across layers (examples of the SSp-bfd and MOp, n = 3 brains).

(E) Distances between the feature distributions (earth-movers distance between the normalized feature distributions). The clustering of the distances reveals 2 major groups of regions, containing preferentially (1) motor and integrative regions (red), and (2) primary and secondary sensory regions (green).

Scale bars represent 1 mm (A), 500 μm (B) and (C), and 200 μm (C, insets). See Table S1 for abbreviations.

We next explored the subcortical relays and found that most of the nuclei of the central auditory pathways in *Otof*$^{-/-}$ mice had lower branching point densities than in control mice. These nuclei included the cochlear nucleus, superior olivary complex, nucleus of the lateral lemniscus and inferior colliculus (Figures 7C and 7D). Although the barrel cortex in *Otof*$^{-/-}$ mice had much higher branch densities than in control mice, the somatosensory relays to the barrel cortex were not affected (Figure 7D), suggesting that cross-modal vascular plasticity was only present in the cortex. Finally, we examined whether the connectivity of capillaries was affected in *Otof*$^{-/-}$ mice by grouping vessels into sub-domains based on the strength of their connections (Figure 7E). We found that although the number of branches was significantly different between the groups in the layers 5 and 4 from the auditory and barrel cortices, respectively, the number of domains was unchanged (Figures 7F and 7G). This finding suggests that the densification of the capillary network may not change vascular territories. Our findings extend the report from (Whiteus et al., 2014) to other brain regions, showing the

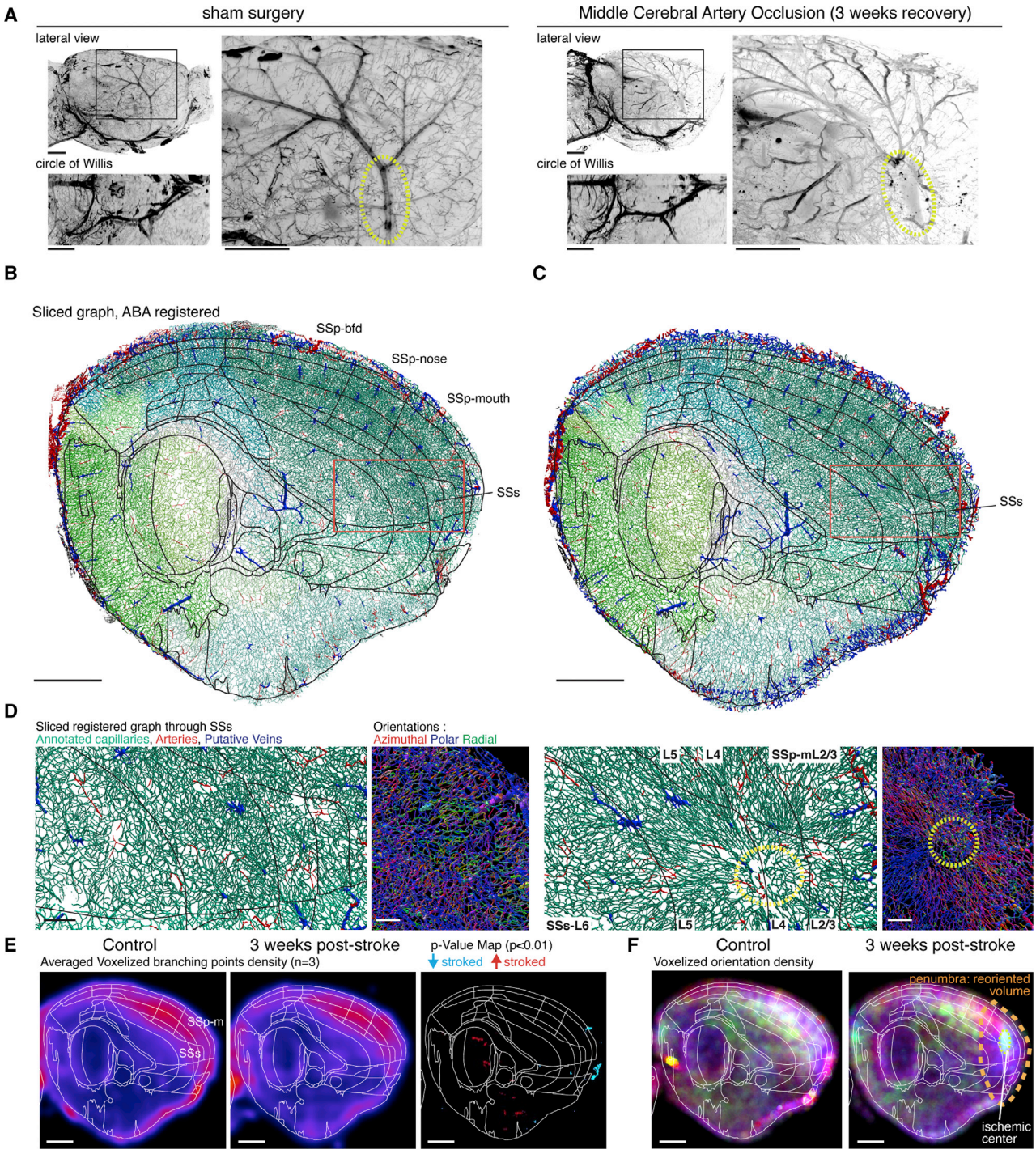

Figure 6. Application of TubeMap to the Study of Ischemic Strokes

(A) Projection of the Acta2 labeling in a control brain or brains recovering for 3 weeks after subjected to an electrocauterization of the middle cerebral artery. Sagittal and ventral projections are shown. The insets show the destruction of the branch (yellow circle) connecting the middle cerebral artery (MCA) dorsal arbor to the circle of Willis.

(B and C) Reconstruction of the vasculature in control (B) and stroked (C) brains. A 250-μm thick sagittal slice through the graph are shown with no noticeable difference in the position and numbers of major veins (in blue) or arteries (red).

(D) Inset from the sliced graph at the level of the supplemental somatosensory (SSs) and mouth primary somatosensory (SSp-m) cortices. Reorientations of the capillaries across layers toward the center of infarct (dotted line) are noticeable in the stroked brain. Color-coding of the vessel orientations reveal a mix of radial (green) and planar (blue and red) orientations in controls, while planar (along the cortical plane) orientations are predominant in the stroked cortex.

(legend continued on next page)

remarkable long-range adaptations enabled by the developmental plasticity of the vascular network.

DISCUSSION

We present a strategy to generate labeled, region-annotated graphs of the mouse brain vasculature. There has been a recent surge of interest in understanding how neuronal function interacts with the cerebral blood flow and how vascular dysfunctions potentiates some pathological states, such as neurodegenerative diseases (Iadecola, 2013; Kisler et al., 2017). Addressing these problems would clearly benefit from the development of image processing pipelines able to cope with the demands of large-scale 3D fluorescence microscopy. Apart from the particular antibody cocktail, our method is not specific to the brain vasculature. Also, other tubular structures could be mapped: nephrons, lung bronchioles, seminiferous tubules, lymphatic system, etc. Indeed, we purposely designed the pipeline on a complex set of principled filters instead of deep neural networks (reserving the latter just for the binary tube-filling application), facilitating its tuning to variations in acquisition parameters or other types of biological objects, adaptations that may be more difficult with a trained network (Belthangady and Royer, 2019).

We validated the combination of 3 markers (podocalyxin, Acta1, and vWF) to discriminate veins, arteries, and capillaries. However, we did not use the data obtained from quadruple channels imaging in our analysis due to important chromatic shifts in light sheet focus and curvature across such a wide range of wavelengths. Therefore, our method would benefit from next-generation light sheet microscopes that improve on resolution and/or acquisition speed (Chakraborty et al., 2019; Pende et al., 2018; Tomer et al., 2014; Voigt et al., 2019). Because access to such microscopes is still limited for most laboratories, we propose here a framework for precise reconstructions with high-throughput and accuracy on commercially available systems. Our method fails to correctly segment and label the pial and meningeal vasculature at the surface of the brain, due to the close apposition of veins and arteries in this planar network. Increasing the imaging resolution may not be sufficient to address errors in arterio-venous junctions visible at the surface of our graphs. Combining our method with high resolution imaging of the blood flow with fast ultrasounds (fUS) (Errico et al., 2015; Hingot et al., 2019) could solve this issue by merging flow-based reconstructions of large vessels with our graphs, while at the same time adding speed and direction information on vessel branches.

The throughput and reliability of the method in generating vascular graphs implies broad possibilities for expanding and revisiting the role of the vasculature in neural functions and pathology. The pipeline lowers the technical barrier to address difficult questions, such as the mechanisms controlling the plasticity of the vasculature in the postnatal brain. Our analysis of a model of ischemic stroke revealed a deep re-orientation of the capillaries toward the anoxic site, an effect that has been documented in other models, such as traumatic brain injury (Cao et al., 2015; Gama Sosa et al., 2019). However, although the addition of new endothelial cells to cerebral vessels has been reported in models of ischemic strokes (Liu et al., 2014; Zhang et al., 2002), we did not measure an increase in branch point density 3 weeks after the stroke away from the site suggesting that the reorganization of the vasculature following hypoxia at a distance from the infarct may involve density-preserving remodeling.

In contrast, we measured opposite effects in a model of activity-dependent developmental plasticity. In congenitally deaf mice, we noted a change in the vascular density that does not affect the size and numbers of capillary territories. Sensory deprivation is known to trigger in the cortex cross-modal compensation in neuronal activity levels, usually by lifting long-range inhibition (He et al., 2012). We could measure this effect by Fos mapping after whisker trimming, which led to an increase in Fos^+ cells density in the auditory cortex (Renier et al., 2016). Much is left to do to characterize the rules of activity-dependent vascular plasticity in the brain, and our tool should facilitate this line of inquiry, because it enables the detection of subtle effects over distant regions. Moreover, the plasticity of the vascular network is intimately linked with neuronal developmental and adult plasticity (Paredes et al., 2018). Our tools will help illuminate topological remodeling of both networks in the developing and adult brains.

To further elucidate the plasticity of the vascular network topology, our method enables the molecular annotation of vessel branches on top of the reconstructed network. This annotation will be invaluable to quantify heterogeneity in marker expression in the endothelium and surrounding cells. For instance, a novel population of $Pdgfra^+$ fibroblasts located in the Virchow-Robin perivascular spaces of arteries and veins has recently been described (Vanlandewijck et al., 2018). Interestingly, these cells express the marker LAMA1 when associated with the vasculature, which could provide an extra marker to discriminate veins in combination with Acta2. As an extension, and because it is based on immunolabeling with/without intracardiac fixative perfusion, our method could also be used to map the expression of markers of pericytes, inflammation, Aß deposits, hypoxia or pathogens on vessel branches, the location of resident immune cells, and microglia close to the vasculature throughout the brain.

Finally, the pipeline could also help investigate the relationship between neuronal networks dysfunctions and metabolism. The implication of a vascular component has been suggested for several disorders affecting higher cognitive functions such as autism (Azmitia et al., 2016), schizophrenia (Hanson and Gottesman, 2005), or obesity (Dorrance et al., 2014). However, the technical demands and time-cost for evaluating the link between

(E) Averaged voxelized branch densities measured from the registered graphs of controls or post-ischemic brains (3 weeks), and the p value map (0.01) of their differences (Mann-Whitney test on voxels, n = 3). No statistically significant changes are observed between the groups.
(F) Voxelized branch orientations, 1 representative example of 3 shown. In the control brain, a mix of all orientations can be seen in the cortex, whereas in the post-ischemic brain, a decrease of radial orientations (green) is seen far from the ischemic site (dotted circle).
Scale bars represent 1 mm, except in (D) (300 μm).

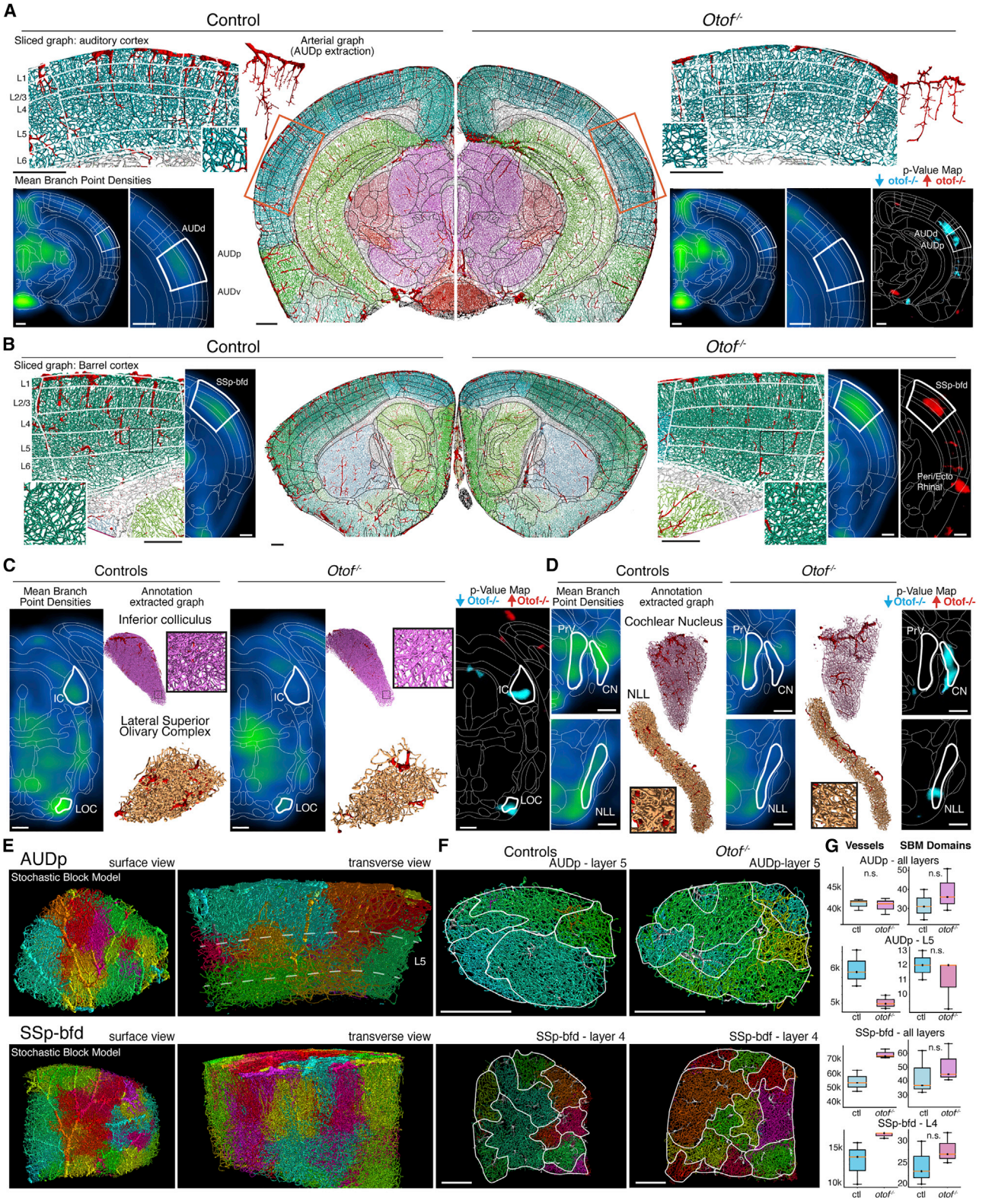

(legend on next page)

vascular development/remodeling and neuronal function is daunting. Our technique provides a new powerful tool of investigation by making large-scale comparisons of vascular topology in disease models accessible.

STAR★METHODS

Detailed methods are provided in the online version of this paper and include the following:

- KEY RESOURCES TABLE
- LEAD CONTACT AND MATERIALS AVAILABILITY
- EXPERIMENTAL MODEL AND SUBJECT DETAILS
  - Animals
- METHOD DETAILS
  - Perfusion and tissue processing
  - Samples staining and iDISCO+ clearing
  - Blood retention
  - Ischemic stroke
  - Light sheet imaging
  - Computing resources
  - WobblyStitcher
  - ClearMap 2.0 toolbox
  - TubeMap pipeline
  - Deep vessel filling
  - Binary smoothing
  - Skeletonization and graph construction
- QUANTIFICATION AND STATISTICAL ANALYSIS
  - Statistical analysis
  - Branch point density, branch density, branch length and tortuosity
  - Shortest paths to arteries and veins
  - Arterial domains
  - Distances of vasculature graph features between cortical regions
  - Stochastic block model analysis
- DATA AND CODE AVAILABILITY

SUPPLEMENTAL INFORMATION

Supplemental Information can be found online at https://doi.org/10.1016/j.cell.2020.01.028.

ACKNOWLEDGMENTS

The authors are grateful to Carl Modes (MPI Dresden); Marcelo Magnasco and Tobias Neubauer (Rockefeller University); Franca Schmid; Bruno Weber (University of Zurich); Alain Chédotal (Vision Institute), Benjamin Charlier, Stanley Durrleman, Laurent Jacob and Jean-Léon Thomas (ICM); and Saaid Safieddine and Christine Petit (Institut Pasteur) for insightful discussions. The authors would also like to thank Patricia Gaspar, Silvina Diaz, and Pablo Ariel for their critical reading of the manuscript, as well as Isabelle Bardet, Marie-Claire Camena d'Almeida, and Antoine Renier for their support throughout the project. This work was also made possible by the ICM.Quant imaging core facility (ICM Brain and Spine Institute), in particular with assistance from Basile Gurchenkov and Aymeric Millecamps. This work was supported by the program "Investissements d'avenir" ANR-10-IAIHU-06, the ERC starter grant "NeuroRemod" (EU Horizon 2020 research program under grant agreement 758817), and the "Paris Emergences" program awarded to N.R. C.K. was supported by an independent research fellowship from the Kavli Neural Systems Institute and by an independent physics fellowship from the Center for Physics and Biology at the Rockefeller University. S.S. is supported by the Région Ile-de-France DIM Math'Innov. A.V.-P. is a Marie Sklodowska Curie Action fellow (Marie Skłodowska-Curie grant 845685). N.M. is supported by grants from the ANR as part of the second Investissements d'Avenir program LIGHT4DEAF (ANR-15-RHUS-0001) and LabEx LIFESENSES (ANR-10-LABX-65), LHW-Stiftung, and by the Prix Emergence of the Fondation pour l'Audition.

AUTHORS CONTRIBUTIONS

C.K., S.S., A.V.-P., T.T., N.M., M.T.-L., and N.R. designed the study. C.K. wrote TubeMap. S.S. implemented the DNN. A.V.-P. and T.T. performed the experiments. G.G. and P.T. performed the ischemic strokes. C.K., S.S., A.V.-P., P.B., and N.R. analyzed the data. F.V. performed the data annotation. N.R. wrote the initial draft of the manuscript. C.K., S.S., and A.V.-P. contributed sections to the manuscript. All co-authors edited the text.

DECLARATION OF INTERESTS

The authors declare no competing interests.

Received: July 31, 2019
Revised: November 20, 2019
Accepted: January 21, 2020
Published: February 13, 2020

REFERENCES

Adams, M.D., Winder, A.T., Blinder, P., and Drew, P.J. (2018). The pial vasculature of the mouse develops according to a sensory-independent program. Sci. Rep. *8*, 9860.

Figure 7. Brain-wide Reorganization of the Vasculature in a Model of Deafness

(A) Sliced graph in coronal orientation at the level of the primary auditory cortex in controls (left) and otoferlin mutant mice (right). Graphs of the auditory cortex arteries are shown. A reduction in the vessel density in the layer 4 of the auditory cortex in the mutant is visible in the mean voxelized branch densities (p value map: $p < 0.01$, Mann-Whitney test, $n = 3$).

(B) Sliced graph at the level of the somatosensory barrel cortex. A higher density of vessels is visible in the mutant barrel cortex in the mean voxelized branch densities ($n = 3$, $p < 0.01$, Mann-Whitney test).

(C) Mean branch densities and graphs of subcortical sensory relays are shown for the inferior colliculus, superior olivary complex, nucleus of the lateral lemniscus, and cochlear nucleus.

(D) While the cochlear nucleus shows a reduction in branch densities, the somatosensory trigeminal principal nucleus (PrV) is not significantly different between control and otoferlin mutant mice.

(E) Sub-domains of vessels inferred in the auditory cortex (AUDp) or barrel cortex (SSp-bfd) of control mice using a stochastic block model (SBM). A sub-domain represents a group of vessels stronger connected to each other than to vessels from another sub-domain. Vessels belonging to the same domain are colored in matching colors.

(F) Views of the domains in layers 5 and 4 of the AUDp and SSp-bdf, respectively, in control or mutant mice.

(G) Number of SBM sub-domains and vessel branches in mutant and control mice for AUDp and SSp-bdf. Results are presented across all cortical layers, or only layer 5 (L5) or 4 (L4). Otoferlin mutant mice show the same number of domains on average than controls, but the number of edges per domain changes in different regions ($n = 3$, Mann-Whitney test). Scale bars are 500 μm.

Ances, B.M. (2004). Coupling of changes in cerebral blood flow with neural activity: what must initially dip must come back up. J. Cereb. Blood Flow Metab. *24*, 1–6.

Arango-Lievano, M., Boussadia, B., De Terdonck, L.D.T., Gault, C., Fontanaud, P., Lafont, C., Mollard, P., Marchi, N., and Jeanneteau, F. (2018). Topographic Reorganization of Cerebrovascular Mural Cells under Seizure Conditions. Cell Rep. *23*, 1045–1059.

Ariel, P. (2018). UltraMicroscope II – A User Guide (University of North Carolina at Chapel Hill, University Libraries).

Ashrafi, G., and Ryan, T.A. (2017). Glucose metabolism in nerve terminals. Curr. Opin. Neurobiol. *45*, 156–161.

Azmitia, E.C., Saccomano, Z.T., Alzoobaee, M.F., Boldrini, M., and Whitaker-Azmitia, P.M. (2016). Persistent Angiogenesis in the Autism Brain: An Immunocytochemical Study of Postmortem Cortex, Brainstem and Cerebellum. J. Autism Dev. Disord. *46*, 1307–1318.

Bates, R., Irving, B., Markelc, B., Kaeppler, J., Brown, G., Muschel, R.J., Brady, S.M., Grau, V., and Schnabel, J.A. (2019). Segmentation of Vasculature From Fluorescently Labeled Endothelial Cells in Multi-Photon Microscopy Images. IEEE Trans. Med. Imaging *38*, 1–10.

Begley, D.J., and Brightman, M.W. (2003). Structural and functional aspects of the blood-brain barrier. Prog. Drug Res. *61*, 39–78.

Belthangady, C., and Royer, L.A. (2019). Applications, promises, and pitfalls of deep learning for fluorescence image reconstruction. Nat. Methods *16*, 1215–1225.

Blinder, P., Tsai, P.S., Kaufhold, J.P., Knutsen, P.M., Suhl, H., and Kleinfeld, D. (2013). The cortical angiome: an interconnected vascular network with noncolumnar patterns of blood flow. Nat. Neurosci. *16*, 889–897.

Breckwoldt, M.O., Bode, J., Kurz, F.T., Hoffmann, A., Ochs, K., Ott, M., Deumelandt, K., Krüwel, T., Schwarz, D., Fischer, M., et al. (2016). Correlated magnetic resonance imaging and ultramicroscopy (MR-UM) is a tool kit to assess the dynamics of glioma angiogenesis. eLife *5*, e11712.

Bria, A., and Iannello, G. (2012). TeraStitcher - a tool for fast automatic 3D-stitching of teravoxel-sized microscopy images. BMC Bioinformatics *13*, 316.

Brunet, I., Gordon, E., Han, J., Cristofaro, B., Broqueres-You, D., Liu, C., Bouvrée, K., Zhang, J., Toro, R., Mathivet, T., et al. (2014). Netrin-1 controls sympathetic arterial innervation. The Journal of Clinical Investigation. https://doi.org/10.1172/jci75181.

Cao, Y., Wu, T., Yuan, Z., Li, D., Ni, S., Hu, J., and Lu, H. (2015). Three-dimensional imaging of microvasculature in the rat spinal cord following injury. Sci. Rep. *5*, 12643.

Chakraborty, T., Driscoll, M.K., Jeffery, E., Murphy, M.M., Roudot, P., Chang, B.-J., Vora, S., Wong, W.M., Nielson, C.D., Zhang, H., et al. (2019). Light-sheet microscopy of cleared tissues with isotropic, subcellular resolution. Nat. Methods *16*, 1109–1113.

Craigie, E.H. (1945). The architecture of the cerebral capillary bed. Biol. Rev. Camb. Philos. Soc. *20*, 133–146.

d'Esposito, A., Sweeney, P.W., Ali, M., Saleh, M., Ramasawmy, R., Roberts, T.A., Agliardi, G., Desjardins, A., Lythgoe, M.F., Pedley, R.B., et al. (2018). Computational fluid dynamics with imaging of cleared tissue and of in vivo perfusion predicts drug uptake and treatment responses in tumours. Nat. Biomed. Eng. *2*, 773–787.

Di Giovanna, A.P., Tibo, A., Silvestri, L., Müllenbroich, M.C., Costantini, I., Allegra Mascaro, A.L., Sacconi, L., Frasconi, P., and Pavone, F.S. (2018). Whole-Brain Vasculature Reconstruction at the Single Capillary Level. Sci. Rep. *8*, 12573.

Dorrance, A.M., Matin, N., and Pires, P.W. (2014). The effects of obesity on the cerebral vasculature. Curr. Vasc. Pharmacol. *12*, 462–472.

Errico, C., Pierre, J., Pezet, S., Desailly, Y., Lenkei, Z., Couture, O., and Tanter, M. (2015). Ultrafast ultrasound localization microscopy for deep super-resolution vascular imaging. Nature *527*, 499–502.

Frangi, A.F., Niessen, W.J., Vincken, K.L., and Viergever, M.A. (1998). In Multiscale Vessel Enhancement Filtering, W.M. Wells, A. Colchester, and S. Delp, eds. (Springer Berlin Heidelberg), pp. 130–137.

Gama Sosa, M.A., De Gasperi, R., Perez Garcia, G.S., Perez, G.M., Searcy, C., Vargas, D., Spencer, A., Janssen, P.L., Tschiffely, A.E., McCarron, R.M., et al. (2019). Low-level blast exposure disrupts gliovascular and neurovascular connections and induces a chronic vascular pathology in rat brain. Acta Neuropathol. Commun. *7*, 6.

Girouard, H., and Iadecola, C. (2006). Neurovascular coupling in the normal brain and in hypertension, stroke, and Alzheimer disease. J. Appl. Physiol. *100*, 328–335.

Hanson, D.R., and Gottesman, I.I. (2005). Theories of schizophrenia: a genetic-inflammatory-vascular synthesis. BMC Med. Genet. *6*, 7.

Harb, R., Whiteus, C., Freitas, C., and Grutzendler, J. (2013). In vivo imaging of cerebral microvascular plasticity from birth to death. J. Cereb. Blood Flow Metab. *33*, 146–156.

He, K., Petrus, E., Gammon, N., and Lee, H.-K. (2012). Distinct sensory requirements for unimodal and cross-modal homeostatic synaptic plasticity. J. Neurosci. *32*, 8469–8474.

Hill, R., Tong, L., Yuan, P., Murikinati, S., Gupta, S., and Grutzendler, J. (2015). Regional Blood Flow in the Normal and Ischemic Brain Is Controlled by Arteriolar Smooth Muscle Cell Contractility and Not by Capillary Pericytes. Neuron *87*, 95–110.

Hingot, V., Errico, C., Heiles, B., Rahal, L., Tanter, M., and Couture, O. (2019). Microvascular flow dictates the compromise between spatial resolution and acquisition time in Ultrasound Localization Microscopy. Sci. Rep. *9*, 2456.

Holland, P.W., Laskey, K.B., and Leinhardt, S. (1983). Stochastic blockmodels: First steps. Soc. Networks *5*, 109–137.

Hörl, D., Rojas Rusak, F., Preusser, F., Tillberg, P., Randel, N., Chhetri, R.K., Cardona, A., Keller, P.J., Harz, H., Leonhardt, H., et al. (2019). BigStitcher: reconstructing high-resolution image datasets of cleared and expanded samples. Nat. Methods *16*, 870–874.

Horvat, R., Hovorka, A., Dekan, G., Poczewski, H., and Kerjaschki, D. (1986). Endothelial cell membranes contain podocalyxin–the major sialoprotein of visceral glomerular epithelial cells. J. Cell Biol. *102*, 484–491.

Iadecola, C. (2013). The pathobiology of vascular dementia. Neuron *80*, 844–866.

Jing, D., Zhang, S., Luo, W., Gao, X., Men, Y., Ma, C., Liu, X., Yi, Y., Bugde, A., Zhou, B.O., et al. (2018). Tissue clearing of both hard and soft tissue organs with the PEGASOS method. Cell Res. *28*, 803–818.

Jonker, R., and Volgenant, A. (1987). A shortest augmenting path algorithm for dense and sparse linear assignment problems. Computing *38*, 325–340.

Keller, A.L., Schüz, A., Logothetis, N.K., and Weber, B. (2011). Vascularization of cytochrome oxidase-rich blobs in the primary visual cortex of squirrel and macaque monkeys. J. Neurosci. *31*, 1246–1253.

Kisler, K., Nelson, A.R., Montagne, A., and Zlokovic, B.V. (2017). Cerebral blood flow regulation and neurovascular dysfunction in Alzheimer disease. Nat. Rev. Neurosci. *18*, 419–434.

Klein, S., Staring, M., Murphy, K., Viergever, M.A., and Pluim, J.P.W. (2010). elastix: a toolbox for intensity-based medical image registration. IEEE Trans. Med. Imaging *29*, 196–205.

Kleinfeld, D., Bharioke, A., Blinder, P., Bock, D., Briggman, K., Chklovskii, D., Denk, W., Helmstaedter, M., Kaufhold, J., Lee, W., et al. (2011). Large-Scale Automated Histology in the Pursuit of Connectomes. Journal of Neuroscience *31*, 16125–16138.

Lacoste, B., Comin, C.H., Ben-Zvi, A., Kaeser, P.S., Xu, X., Costa, Lda.F., and Gu, C. (2014). Sensory-related neural activity regulates the structure of vascular networks in the cerebral cortex. Neuron *83*, 1117–1130.

Lagerweij, T., Dusoswa, S.A., Negrean, A., Hendrikx, E.M.L., de Vries, H.E., Kole, J., Garcia-Vallejo, J.J., Mansvelder, H.D., Vandertop, W.P., Noske, D.P., et al. (2017). Optical clearing and fluorescence deep-tissue imaging for 3D quantitative analysis of the brain tumor microenvironment. Angiogenesis *20*, 533–546.

Liebmann, T., Renier, N., Bettayeb, K., Greengard, P., Tessier-Lavigne, M., and Flajolet, M. (2016). Three-Dimensional Study of Alzheimer's Disease Hallmarks Using the iDISCO Clearing Method. Cell Rep. *16*, 1138–1152.

Liu, J., Wang, Y., Akamatsu, Y., Lee, C.C., Stetler, R.A., Lawton, M.T., and Yang, G.-Y. (2014). Vascular remodeling after ischemic stroke: mechanisms and therapeutic potentials. Prog. Neurobiol. *115*, 138–156.

Livne, M., Rieger, J., Aydin, O.U., Taha, A.A., Akay, E.M., Kossen, T., Sobesky, J., Kelleher, J.D., Hildebrand, K., Frey, D., and Madai, V.I. (2019). A U-Net Deep Learning Framework for High Performance Vessel Segmentation in Patients With Cerebrovascular Disease. Front. Neurosci. *13*, 97.

Llovera, G., Roth, S., Plesnila, N., Veltkamp, R., and Liesz, A. (2014). Modeling stroke in mice: permanent coagulation of the distal middle cerebral artery. J. Vis. Exp. *89*, e51729.

Lu, H., Wang, Y., He, X., Yuan, F., Lin, X., Xie, B., Tang, G., Huang, J., Tang, Y., Jin, K., et al. (2012). Netrin-1 hyperexpression in mouse brain promotes angiogenesis and long-term neurological recovery after transient focal ischemia. Stroke *43*, 838–843.

Lugo-Hernandez, E., Squire, A., Hagemann, N., Brenzel, A., Sardari, M., Schlechter, J., Sanchez-Mendoza, E.H., Gunzer, M., Faissner, A., and Hermann, D.M. (2017). 3D visualization and quantification of microvessels in the whole ischemic mouse brain using solvent-based clearing and light sheet microscopy. J. Cereb. Blood Flow Metab. *37*, 3355–3367.

Mächler, P., Wyss, M.T., Elsayed, M., Stobart, J., Gutierrez, R., von Faber-Castell, A., Kaelin, V., Zuend, M., San Martín, A., Romero-Gómez, I., et al. (2016). In Vivo Evidence for a Lactate Gradient from Astrocytes to Neurons. Cell Metab. *23*, 94–102.

Michaloudi, H., Grivas, I., Batzios, C., Chiotelli, M., and Papadopoulos, G.C. (2005). Areal and laminar variations in the vascularity of the visual, auditory, and entorhinal cortices of the developing rat brain. Brain Res. Dev. Brain Res. *155*, 60–70.

Michalski, N., Goutman, J.D., Auclair, S.M., Boutet de Monvel, J., Tertrais, M., Emptoz, A., Parrin, A., Nouaille, S., Guillon, M., Sachse, M., et al. (2017). Otoferlin acts as a Ca^{2+} sensor for vesicle fusion and vesicle pool replenishment at auditory hair cell ribbon synapses. eLife *6*, e31013.

Müller, N., Sonntag, M., Maraslioglu, A., Hirtz, J., and Friauf, E. (2019). Topographic map refinement and synaptic strengthening of a sound localization circuit require spontaneous peripheral activity. The Journal of Physiology *597*, 5469–5493.

Németh, G., Kardos, P., and Palágyi, K. (2010). Topology Preserving Parallel Smoothing for 3D Binary Images. In Computational Modeling of Objects Represented in Images, R.P. Barneva, V.E. Brimkov, H.A. Hauptman, R.M. Natal Jorge, and J.M.R.S. Tavares, eds. (Springer Berlin Heidelberg), pp. 287–298.

Newman, P.J., Berndt, M.C., Gorski, J., White, G.C., 2nd, Lyman, S., Paddock, C., and Muller, W.A. (1990). PECAM-1 (CD31) cloning and relation to adhesion molecules of the immunoglobulin gene superfamily. Science *247*, 1219–1222.

Palágyi, K., and Kuba, A. (1999). A Parallel 3D 12-Subiteration Thinning Algorithm. Graph. Models Image Proc. *61*, 199–221.

Paredes, I., Himmels, P., and Ruiz de Almodóvar, C. (2018). Neurovascular Communication during CNS Development. Dev. Cell *45*, 10–32.

Peixoto, T.P. (2014). Hierarchical Block Structures and High-Resolution Model Selection in Large Networks. arXiv, arXiv:1310.4377.

Peixoto, T.P. (2017). Nonparametric Bayesian inference of the microcanonical stochastic block model. Phys. Rev. E *95*, 12317.

Pende, M., Becker, K., Wanis, M., Saghafi, S., Kaur, R., Hahn, C., Pende, N., Foroughipour, M., Hummel, T., and Dodt, H.-U. (2018). High-resolution ultramicroscopy of the developing and adult nervous system in optically cleared Drosophila melanogaster. Nat. Commun. *9*, 4731.

Quintana, D.D., Lewis, S.E., Anantula, Y., Garcia, J.A., Sarkar, S.N., Cavendish, J.Z., Brown, C.M., and Simpkins, J.W. (2019). The cerebral angiome: High resolution MicroCT imaging of the whole brain cerebrovasculature in female and male mice. Neuroimage *202*, 116109.

Renier, N., Adams, E.L., Kirst, C., Wu, Z., Azevedo, R., Kohl, J., Autry, A.E., Kadiri, L., Umadevi Venkataraju, K., Zhou, Y., et al. (2016). Mapping of Brain Activity by Automated Volume Analysis of Immediate Early Genes. Cell *165*, 1789–1802.

Ridler, T.W., and Calvard, S. (1978). Picture thresholding using an iterative selection method. IEEE Trans. Syst. Man. Cybern. *8*, 630–632.

Roche, M., Chaigneau, E., Rungta, R.L., Boido, D., Weber, B., and Charpak, S. (2019). In vivo imaging with a water immersion objective affects brain temperature, blood flow and oxygenation. eLife *8*, e47324.

Roux, I., Safieddine, S., Nouvian, R., Grati, M., Simmler, M.-C., Bahloul, A., Perfettini, I., Le Gall, M., Rostaing, P., Hamard, G., et al. (2006). Otoferlin, defective in a human deafness form, is essential for exocytosis at the auditory ribbon synapse. Cell *127*, 277–289.

Sato, Y., Nakajima, S., Shiraga, N., Atsumi, H., Yoshida, S., Koller, T., Gerig, G., and Kikinis, R. (1998). Three-dimensional multi-scale line filter for segmentation and visualization of curvilinear structures in medical images. Med. Image Anal. *2*, 143–168.

Schmid, F., Barrett, M.J.P., Jenny, P., and Weber, B. (2019). Vascular density and distribution in neocortex. Neuroimage *197*, 792–805.

Tamura, A., Graham, D.I., McCulloch, J., and Teasdale, G.M. (1981). Focal cerebral ischaemia in the rat: 1. Description of technique and early neuropathological consequences following middle cerebral artery occlusion. J. Cereb. Blood Flow Metab. *1*, 53–60.

Testa, J.E., Chrastina, A., Li, Y., Oh, P., and Schnitzer, J.E. (2009). Ubiquitous yet distinct expression of podocalyxin on vascular surfaces in normal and tumor tissues in the rat. J. Vasc. Res. *46*, 311–324.

Tetteh, G., Efremov, V., Forkert, N.D., Schneider, M., Kirschke, J., Weber, B., Zimmer, C., Piraud, M., and Menze, B.H. (2018). Deepvesselnet: Vessel segmentation, centerline prediction, and bifurcation detection in 3-d angiographic volumes. arXiv, arXiv:1803.09340.

Todorov, M.I., Paetzold, J.C., Schoppe, O., Tetteh, G., Efremov, V., Völgyi, K., Düring, M., Dichgans, M., Piraud, M., Menze, B., and Ertürk, A. (2019). Automated analysis of whole brain vasculature using machine learning. bioRxiv. https://doi.org/10.1101/613257.

Tomer, R., Ye, L., Hsueh, B., and Deisseroth, K. (2014). Advanced CLARITY for rapid and high-resolution imaging of intact tissues. Nat. Protoc. *9*, 1682–1697.

Tsai, P.S., Kaufhold, J.P., Blinder, P., Friedman, B., Drew, P.J., Karten, H.J., Lyden, P.D., and Kleinfeld, D. (2009). Correlations of neuronal and microvascular densities in murine cortex revealed by direct counting and colocalization of nuclei and vessels. J. Neurosci. *29*, 14553–14570.

Vanlandewijck, M., He, L., Mäe, M.A., Andrae, J., Ando, K., Del Gaudio, F., Nahar, K., Lebouvier, T., Laviña, B., Gouveia, L., et al. (2018). A molecular atlas of cell types and zonation in the brain vasculature. Nature *554*, 475–480.

Voigt, F.F., Kirschenbaum, D., Platonova, E., Pagès, S., Campbell, R.A.A., Kästli, R., Schaettin, M., Egolf, L., van der Bourg, A., Bethge, P., et al. (2019). The mesoSPIM initiative: open-source light-sheet microscopes for imaging cleared tissue. Nat. Methods *16*, 1105–1108.

Whiteus, C., Freitas, C., and Grutzendler, J. (2014). Perturbed neural activity disrupts cerebral angiogenesis during a postnatal critical period. Nature *505*, 407–411.

Yasunaga, S., Grati, M., Cohen-Salmon, M., El-Amraoui, A., Mustapha, M., Salem, N., El-Zir, E., Loiselet, J., and Petit, C. (1999). A mutation in OTOF, encoding otoferlin, a FER-1-like protein, causes DFNB9, a nonsyndromic form of deafness. Nat. Genet. *21*, 363–369.

Zhang, L.-Y., Lin, P., Pan, J., Ma, Y., Wei, Z., Jiang, L., Wang, L., Song, Y., Wang, Y., Zhang, Z., et al. (2018). CLARITY for High-resolution Imaging and Quantification of Vasculature in the Whole Mouse Brain. Aging Dis. *9*, 262–272.

Zhang, Z., Zhang, L., Jiang, Q., and Chopp, M. (2002). Bone marrow-derived endothelial progenitor cells participate in cerebral neovascularization after focal cerebral ischemia in the adult mouse. Circulation Research *90*, 284–288.

Zlokovic, B.V. (2008). The blood-brain barrier in health and chronic neurodegenerative disorders. Neuron *57*, 178–201.

Zlokovic, B.V. (2011). Neurovascular pathways to neurodegeneration in Alzheimer's disease and other disorders. Nat. Rev. Neurosci. *12*, 723–738.

STAR★METHODS

KEY RESOURCES TABLE

REAGENT or RESOURCE	SOURCE	IDENTIFIER
Antibodies		
Rat anti-Podocalyxin Dilution 1:1000	R and D Systems	Cat#MAB1556 RRID: AB_2166010, Lot: IPF0317101
Goat anti-Podocalyxin Dilution 1:1500	R and D Systems	Cat# AF1556, RRID: AB_354858, Lot: JPC0118101
Goat anti-CD31/PCAM-1 Dilution 1:300	R and D Systems	Cat#AF3628 RRID: AB_2161028, Lot: YZU0118051
Goat anti-alpha smooth muscle actin Dilution 1:1500	Abcam	Cat# ab21027, RRID: AB_1951138, Lot: GR372483-1
Goat anti-alpha smooth muscle actin Dilution 1:1500	Novus	Cat# NB300-978, RRID: AB_2273630, Lot: 84C262p13
Rabbit anti-alpha smooth muscle actin Dilution 1:1000	Abcam	Cat#ab5694 RRID: AB_2223021, Lots: GR3263275-2, GF3183259-11
Rabbit anti-TRANSGELIN/SM22 Dilution 1:1500	Abcam	Cat# ab14106, RRID: AB_443021, Lot: GR3247382-1
Rabbit anti-TRANSGELIN/SM22 Dilution 1:300	Proteintech	Cat# 10493-1-AP, RRID: AB_219936, Lot: 00040337
Rabbit anti-CollagenIV Dilution 1:1000	Abcam	Cat#ab19808 RRID: AB_445160, Lot: GR261208-23
Rabbit anti-Human Von Willebrand Factor Dilution 1:300	Agilent	Cat#A0082, RRID: AB_2315602, Lot: 20067358
Donkey anti-Goat IgG (H+L) Cross-Adsorbed Secondary Antibody, Alexa Fluor 647 Dilution 1:500	Thermo Fisher Scientific	Cat# A-21447, RRID: AB_2535864, Lot: multiple
Donkey anti-Goat IgG (H+L) Cross-Adsorbed Secondary Antibody, Alexa Fluor 555 Dilution 1:500	Thermo Fisher Scientific	Cat# A-21432, RRID: AB_2535853, Lot: multiple
Goat anti-Rat IgG (H+L) Cross-Adsorbed Secondary Antibody, Alexa Fluor 647 Dilution 1:500	Thermo Fisher Scientific	Cat# A-21247, RRID: AB_141778, Lot: multiple
Chicken anti-Rat IgG (H+L) Cross-Adsorbed Secondary Antibody, Alexa Fluor 647 Dilution 1:500	Thermo Fisher Scientific	Cat# A-21472, RRID: AB_2535875, Lot: multiple
Donkey anti-Rabbit IgG (H+L) Highly Cross-Adsorbed Secondary Antibody, Alexa Fluor 647 Dilution 1:500	Thermo Fisher Scientific	Cat# A-31573, RRID: AB_2536183, Lot: multiple
Donkey anti-Rabbit IgG (H+L) Highly Cross-Adsorbed Secondary Antibody, Alexa Fluor 555 Dilution 1:500	Thermo Fisher Scientific	Cat# A-31572, RRID: AB_162543, Lot: multiple
Donkey anti-Mouse IgG (H+L) Highly Cross-Adsorbed Secondary Antibody, Alexa Fluor 647 Dilution 1:500	Thermo Fisher Scientific	Cat# A-31571, RRID: AB_162542, Lot: multiple
Rabbit anti-Neurofilament M dilution 1:1000	Biolegend	Cat# 841001, RRID: AB_2565457, Lot: B244512
Chicken anti-Glial Fibrillary Acidic Protein (GFAP) dilution 1:1000	Aves	Cat# GFAP, RRID: AB_2313547, Lot: GFAP8847982
Experimental Models: Organisms/Strains		
Mouse strain *Otof* $^{Ala515,Ala517/Ala515,Ala517}$	Pasteur Institute	N/A
Mouse strain C57BL6/NRj	Janvier Labs	RRID: MGI:6236253
Mouse strain FVB/NRj	Janvier Labs	MGI:2163709
Software and Algorithms		
Bitplane Imaris 9.2	Oxford Instruments	RRID: SCR_007370
Fiji	NIH	RRID: SCR_002285
ClearMap 2.0 with TubeMap pipeline	This Study	https://github.com/ChristophKirst
ITK-SNAP	NITRC	RRID: SCR_002010

LEAD CONTACT AND MATERIALS AVAILABILITY

Further information and requests for resources and reagents should be directed, and will be fulfilled by the Lead Contact, Nicolas Renier (nicolas.renier@icm-institute.org). This study did not generate new unique reagents.

EXPERIMENTAL MODEL AND SUBJECT DETAILS

Animals

All procedures followed the European legislation for animal experimentation (directive 2010/63/EU). Animal manipulations were approved by the institutional Ethical Committee (Project Ce5/2016/3996). Adult male and female mice were used in the study of C57Bl/N and FVB backgrounds, obtained from Janvier Labs. All the animals were in between 8 and 12 weeks old when the experimental procedures were initiated. Animals were housed in group, in ventilated racks with free access to food and water. Temperature, humidity and photoperiod were controlled.

METHOD DETAILS

Perfusion and tissue processing

All animals were sacrificed by Pentobarbital overdose (200mg/100 g of animal). Intracardiac perfusion was then performed with a peristaltic pump (Gilson, USA). Blood was washed by infusing 30mL of cold PBS followed by tissue fixation with 30mL of cold 4% Paraformaldehyde (Electron Microscopy Sciences, USA) diluted in PBS. Then the brains were quickly dissected taking special care to preserve intact the structure. Finally, the brains were postfixed for 2 hours at room temperature by immersion in 4% Paraformaldehyde, and stored in PBS at 4°C until further processing.

Samples staining and iDISCO+ clearing

Whole brain vasculature staining was performed following the iDISCO+ protocol previously described (Renier et al., 2016) with minimal modifications. All the steps of the protocol were done at room temperature with gentle shaking unless otherwise specified. All the buffers were supplemented with 0,01% Sodium Azide (Sigma-Aldrich, Germany) to prevent bacterial and fungi growth.

Perfused brains were dehydrated in an increasing series of methanol (Sigma-Aldrich, France) dilutions in water (washes of 1 hour in methanol 20%, 40%, 60%, 80% and 100%). An additional wash of 2 hours in methanol 100% was done to remove residual water. Once dehydrated, samples were incubated overnight in a solution containing a 66% dichloromethane (Sigma-Aldrich, Germany) in methanol, and then washed twice in methanol 100% (4 hours each wash). Samples were then bleached overnight at 4°C in methanol containing a 5% of hydrogen peroxide (Sigma-Aldrich). Rehydration was done by incubating the samples in methanol 60%, 40% and 20% (1 hour each wash). After methanol pretreatment, samples were washed in PBS twice 15 minutes, 1 hour in PBS containing a 0,2% of Triton X-100 (Sigma-Aldrich), and further permeabilized by a 24 hours incubation at 37°C in *Permeabilization Solution*, composed by 20% dimethyl sulfoxide (Sigma-Aldrich), 2,3% Glycine (Sigma-Aldrich, USA) in PBS-T. In order to start the immunostaining, samples were first blocked with 0,2% gelatin (Sigma-Aldrich) in PBS-T for 24 hours at 37°C. The same blocking buffer was used to prepare antibody solutions. A combination of primary antibodies targeting different components of the vessel's walls was used to achieve continuous immunostaining. Antibodies to Podocalyxin and CD31 were combined to stain the full capillary net and large veins, while an anti-Alpha Smooth Muscle Actin (αSMA or Acta2) antibody was used to label the artery's wall (antibodies' references and concentrations are provided in the Key Resources Table). Primary antibodies were incubated for 10 days at 37°C with gentle shaking, then washed in PBS-T (twice 1 hour and then overnight), and finally newly incubated for 10 days with secondary antibodies. Secondary antibodies conjugated to Alexa 647 were used to detect Podocalyxin and CD31, while arteries were stained with secondary antibodies conjugated to Alexa 555. After immunostaining, the samples were washed in PBS-T (twice 1 hour and then overnight), dehydrated in a methanol/water increasing concentration series (20%, 40%, 60%, 80%, 100% one hour each and then methanol 100% overnight), followed by a wash in 66% dichloromethane – 33% methanol for 3 hours. Methanol was washed out with two final washes in dichloromethane 100% (15 min each) and finally the samples were cleared and stored in dibenzyl ether (Sigma-Aldrich) until light sheet imaging.

Blood retention

The blood retention experiments were designed to retain as much blood in the vessels as possible while optimizing fixative diffusion in the tissue. These experiments involve a four-day process of dissection and post fixation steps. First, the mice were euthanized with CO2 and their skin was carefully dissected from the neck to the snout, avoiding injury to the surrounding blood vessels, especially the jugular veins. Following the dissection, the animals were placed in 4% Paraformaldehyde (PFA) for post-fixation, at 4°C, overnight. The next day, the interparietal bone was dissected, the snout was removed with surgical scissors, and the animals were again placed in 4% PFA for post-fixation, at 4°C, overnight. On the third day, the brain was dissected and placed again in 4% PFA for a final post-fixation step, at 4°C, overnight. On the fourth day, the brains were washed 4-5 times with 1X phosphate-buffered saline (PBS) and kept at 4°C before further processing.

Ischemic stroke

Ischemic stroke was induced by middle cerebral artery (MCA) electrocoagulation as previously described (Llovera et al., 2014; Tamura et al., 1981). Briefly, animals were deeply anesthetized with isoflurane 5% and maintained with 2.5% isoflurane in a 70%/30% mixture of NO2/O2. Mice were placed in a stereotaxic device, the skin between the right eye and the right ear was incised, and the temporal muscle was retracted. A small craniotomy was performed, the dura was excised, and the middle cerebral artery (MCA) was

exposed. The MCA was electro-coagulated before its bifurcation with bipolar forceps, under irrigation, then the craniotomy, muscle and skin were closed and sutured.

Light sheet imaging

As a compromise between imaging speed and isotropic axial resolution, we imaged with a 4X 0.35NA objective cropped elongated field of view (600 × 2200μm) covering the narrow waist of the light sheet at 1.63μm/pixel of lateral resolution. Increasing the magnification didn't improve the axial resolution (Figure S3C). The planes spacing and cropping factor where optimized to avoid fusion of nearby vessels (Figures S3D–S3F). We observed that this tiling configuration led to a small anisotropy in the measured capillary diameters (Figures S3G and S3H). While shifts between the channels due to chromatic aberration were observed (Figure S3A), corrections were not necessary as the arterial binary image mask still overlap with the vessels binary image mask. This approach yields a near isotropic resolution, while striving to maintain an acquisition time under 1 day per brain (6h per hemisphere per channel) by expanding the width of the FOV over the ideal Rayleigh distance:

$$Z_r = \frac{2\pi \cdot \omega_0^2}{\lambda}$$

where $\omega_0 = (n \cdot \lambda / \pi\, NA)$ is the beam waist. At this NA and 647nm wavelength, Z_r is 100μm.

Tiling the cropped 4X FOV generates between 72 and 91 tiles per hemisphere, between 2900 and 3200 planes at 1.6μm spacing, which yields about 200Gb of uncompressed image files per channel per hemisphere. A reference channel for the registration to the annotated atlas using the sample autofluorescence was acquired at 5μm/pixel. As we are using the very limits of what enables a homogeneous image, it is extremely important that the microscope light sheet beam is well centered in all directions: y position, x,y tilt and planarity.

The acquisitions were done on a LaVision Ultramicroscope II equipped with infinity-corrected objectives. The microscope was installed on an active vibration filtration device, itself put on a marble compressed-air table. Imaging was done with the following filters: 595/40 for Alexa Fluor-555, and −680/30 for Alexa Fluor-647. The microscope was equipped with the following laser lines: OBIS-561nm 100mW, OBIS-639nm 70mW, and used the 2nd generation LaVision beam combiner. The images were acquired with an Andor CMOS sNEO camera. Main acquisitions were done with the LVMI-Fluor 4X/O.3 WD6 LaVision Biotec objective. The microscope was connected to a computer equipped with SSD drives to speed up the acquisition.

The brain was positioned in sagittal orientation, cortex side facing the light sheet, to maximize image quality and consistency. Indeed, while horizontal orientation is possible and enables whole-brain scanning in one acquisition, it is impossible here, as we use 1 light sheet illumination to increase the axial resolution to the maximum (combining 3 or 6 light sheets would be very detrimental to the resolution). Using 1 light sheet illumination in horizontal scan reduces illumination consistency because of 1) Excessive shadows from the white matter tracts 2) Light scattering at the midline of the tissue (see Ariel [2018] for a complete guide and explanations).

A field of view of 400 × 1300 pixels was cropped at the center of the camera sensory. The light sheet numerical aperture was set to the maximal NA (0.1). Beam width was set to the maximum. Only the center-left light sheet was used. Laser powers were set to 100% (639nm) or 40% (561nm). The center of the light sheet in x was carefully calibrated to the center of the field of view using capillaries, which should appear as points, not lines, when the light sheet is centered. z steps were set to 1.6μm. Tile overlaps were set to 10%. The acquisition routine was set to 1) Z-drive - > Save ome.tif stack 2) Filter change - > Z-drive - > Save ome.tif stack 3) Change X position - > repeat 1,2 12 times 4) Change y position - > repeat 1,2,3 6 times. The whole acquisition takes about 14h per hemisphere.

At the end of the acquisition, the objective is changed to a MI PLAN 1.1X/0.1 for the reference scan at 488nm excitation (tissue autofluorescence). The field of view is cropped to the size of the brain, and the z-steps are set to 6μm, and light sheet numerical aperture to 0.03 NA. It is important to crop the field of view to the size of the brain for subsequent alignment steps. After this acquisition (about 3 minutes), the brain is flipped to the other hemisphere and upside-down, so that the cortical side still faces the left light sheet.

The signal-to-noise (SN) ratio was calculated as:

$$\mathrm{SN} = \frac{\max(A) - \mu_B}{\sigma_B}$$

where μ_B is the mean of the background signal, max*(A)* is the peak of signal in the weakest capillaries and σ_B is the standard deviation of the background signal.

Full Width at Half-Max (FWHM) where calculated by fitting Gaussian functions to the profiles of capillaries taken in different location and orientations of the scans.

Computing resources

The data were automatically transferred every day from the acquisition computer to a Lustre server for storage. The processing with TubeMap was done on local workstations, either Dell Precision T7920 or HP Z840. Each workstation was equipped with 2 Intel Xeon Gold 6128 3.4G 6C/12T CPUs, 512Gb of 2666MHz DDR4 RAM, 4x1Tb NVMe Class 40 Solid State Drives in a RAID0 array (plus a

separate system disk), and an NVIDIA Quadro P6000, 24Gb VRAM video card. The workstations were operated by Linux Ubuntu 18.04LTS. TubeMap was used on Anaconda Python 3.6 or Python 2.7 environments.

WobblyStitcher

Our method to acquire isotropic data via light-sheet imaging produces a large number of tiles that have to be aligned and stitched. For accurate reconstruction of the vasculature network at the vasculature capillary level a precise and robust alignment of large datasets is needed.

Existing stitching tools for large datasets could not generate accurate stitching results for our datasets due to misalignments arising from the placement methods (TeraStitcher) or large data reading and writing (BigStitcher). Even for well-placed tiles, rigid stitching produced object duplications in sub-regions along the z-axis indicating x-y movements of the images along this axis. Those movements likely originate from imprecise stage movements and were found on different microscopes and are prevalent in other datasets from other labs (personal communication from Pablo Ariel, University of North Carolina). To solve these problems, we developed WobblyStitcher, an open-source software tool for robust and non-rigid stitching of terabyte datasets.

WobblyStitcher uses three main steps to stitch the data (Figure 1H): (i) alignment, (ii) placement, and (iii) stitching. In the alignment step the non-rigid displacements between images are estimated along with additional quality measures of the alignment reliability. In the placement step a combination of tracking and optimization tools is used to robustly position individual tiles within a global image frame. Finally, the stitching step uses 3D interpolation methods in the overlapping regions to compose the final volumetric image.

The 3D non-rigid alignment is done in three sub-steps: (a) rigid alignment of the tiles along the axis orthogonal to the light sheet plane (z-axis), (b) placement of the tiles along this axis, followed by (c) non-rigid alignments within each plane (x-y-planes).

While a full non-rigid 3D alignment is possible by employing for example non-linear registration methods (e.g., elastix) (Klein et al., 2010) we did not find this necessary for our datasets. Our non-rigid alignment is targeted toward light-sheet images and optimized for fast processing of terabyte-sized datasets. However, the modular architecture of WobblyStitcher is designed for extensions including full 3D non-rigid stitching and will be published elsewhere.

Rigid alignment

In the first step, neighboring tiles are rigidly aligned along the z-axis. To speed up this step, a max-intensity projection (MIP) is calculated along the axis that connects the two tiles and the alignment is performed on the resulting 2d images. While WobblySticher implements full 3d rigid alignment, we did not find this necessary for our datasets in this step and opted for the faster MIP version.

The n-dimensional rigid alignment is done via minimizing the mean square difference between the pixel intensities of two images I_i and I_j over all possible n-dimensional displacements s in the overlap region $O_{ij}(s)$ as

$$s_{ij}^{*} = \underset{s}{\operatorname{argmin}}\, S_{ij}(s)$$

with

$$S_{ij}(s) = \frac{1}{N_{ij}(s)} \sum_{x \in O_{ij}(s)} \left(I_i(x) - I_j(x+s)\right)^2$$

where $N_{ij}(s) = \left|O_{ij}(s)\right|$ is the number of pixels in the overlap. We set $S_{ij}(s) = \infty$ if there is no overlap, i.e., $N_{ij}(s) = 0$. This estimate allows for a fast implementation via Fast Fourier Transform.

WobblyStitcher implements correlation or normalized cross-correlation measures to estimate the shifts. In addition, other more sophisticated measures to estimate the displacements exists (Klein et al., 2010) but are not implemented in WobblyStitcher yet, as we did not find those necessary to align our datasets.

Differences in high intensity voxels will contribute strongly to the error measure S above and can induce unwanted fluctuations, thus WobblyStitcher gives an option to preprocess the images before calculating the alignment. Arbitrary preprocessing routines can be passed. For the brain vasculature preprocessing includes clipping at specified intensity values above a threshold θ_h and below θ_l as well as normalizing the images by subtracting the mean and dividing by the standard deviation in the overlap regions.

In addition, the alignment estimates s_{ij}^{*} can be corrupted in regions without or very little foreground signal as background noise is aligned in this situation. WobblyStitcher provides the option to pass a validation routine to the alignment and to measure the quality of the alignment to prevent this problem. For the brain vasculature the validation is done on the raw data by requiring that the number of foreground pixels in the overlap region exceeds a certain fraction or minimal number of required valid pixels, i.e

$$\left|\left\{\theta_b < x < \theta_t \,|\, x \in O_{ij}(0)\right\}\right| \geq n_v$$

where θ_b and θ_t are intensity thresholds below or above pixels are considered as invalid for alignment.

To measure the quality of the alignments the following measure is used

$$q_{ij}^{*} = \begin{cases} -S\left(s_{ij}^{*}\right) & \text{for valid alignments} \\ -\infty & \text{else.} \end{cases}$$

Optimal rigid placement

Having measured the displacements between all tiles along the z-axis a placement along this axis is performed. For this we use globally optimal placement strategy to find the position p_i for each tile i by minimizing the error term

$$E = \sum_{(i,j)\in P} \left(p_i + s_{ij} - p_j\right)^2$$

with respect to the positions p_i. Here P is the set of pairs of indices (i,j) of all neighboring tiles for which the alignment quality $q^*_{ij} > \theta_q$ exceeded a certain quality threshold θ_q. The resulting set of equations is solved for the positions via the Penrose pseudo inverse. The equations can be solved separately in each coordinate dimension to speed up computation of full 3d rigid placements or to calculate the optimal alignment along a single axis. More importantly, thresholding the alignment quality can force the alignment graph (nodes given by the tiles and edges indicating valid alignment pairs of tiles) to become disconnected. WobblyStitcher accounts for this by optimizing each connected component individually. For the brain vasculature the quality threshold is set to $\theta_q = -\infty$ in the z-alignment step only separating empty tiles from the brain sample.

Non-rigid alignment

In the final step every pair of tiles is aligned non-rigidly in the x-y planes via a series of computations:

First, the overlap region for each pair of neighboring and already z-aligned tiles is computed. The overlap region is validated via an optional validation routine passed to WobblySticher. For the brain vasculature we use foreground pixel counting as described above. The overlap regions are also preprocessed as a whole using normalization.

Second, for each z-value in the overlap region slices of the tiles in the x-y plane are taken and the alignment error S defined above computed for each slice. For the vasculature each slice is validated again separately using raw data slices and a higher threshold for the number of required valid pixels n_v.

Third, the best displacements along the z-axis of the two tiles are determined via tracking. The reason for this step is to achieve robustness against errors that can occur as multiple local minima can arise in the error landscape S in datasets with repetitive structures near the overlap region. When considering global minima alone, this can create jumps in the displacements and errors in the alignments. WobblyStitcher first creates a list of all local minima in the error landscape S (excluding pixel at the overlap border) together with their quality measure q for each x-y-slice. Invalid marked slices will separate continuous segments of valid slices along z. For each continuous segment linear programming (Jonker and Volgenant, 1987) is used to track the local minima resulting in potential displacement paths through z. To find the full path in each segment the longest potential path with best quality measure is selected and all trajectories within that z-range of paths removed. Subsequently, the next longest path with minimal alignment error is selected etc. Valid slices that could not be assigned a displacement in this way will be marked as untraced and invalid.

Fourth, an optional smoothing is applied to the segments of valid displacements along the z-axis. For the vasculature we use convolution with a Bartlett window to smooth the segments.

The total result of this alignment procedure is that tiles become aligned in z and for each neighboring x-y-plane a robust displacement is determined together with markers for validity, quality and traceability.

Final Placement

In this second step the tiles are placed non-rigidly considering the validity and quality of the displacement measure.

WobblyStitcher first use the quality based global optimal alignment method described above to place the individual x-y planes in each z-slice of the entire dataset. For each slice this results in optimal displacements of the connected components. We will refer to each of these connected components in a single plane as a cluster for simplicity in the following.

In the second placement step, clusters are aligned optimally in the entire image. To achieve this the connectivity structure between the clusters is determined first by constructing a graph with clusters as nodes and edges between two clusters if they are from subsequent z-planes and overlap in the x-y-plane. The connected components of clusters in this graph are then aligned, by considering all displacements between the clusters and optimizing the error function:

$$E = \sum_s \sum_{i\in C_{s,i}} \sum_{j\in C_{s+1}} \sum_{k\in C_{s,i}\cap C_{s+1,j}} \left(\left(p_{s,k} + d_{s,i}\right) - \left(p_{s+1,k} + d_{s+1,j}\right)\right)^2$$

with respect to the unknown displacements $d_{s,i}$ for cluster i in slice s. Here C_s is the set of clusters in slice s belonging to the connected component under consideration, $C_{s,i}$ is the index set of all tiles of the cluster i in slice s, and $p_{s,k}$ is the already optimized valid position of the slice s of tile k. The optimization is again performed via the pseudo inverse to solve for the displacements $d_{s,i}$. This results in optimal cluster positions and consequently in optimal positions of the individual image planes.

In a post-processing step, segments of untraceable or invalid slices of tiles that are neighboring valid slices in the z-axis are positioned using linear interpolation between the positions of the valid slices. Finally, the displacements along the z-axis are smoothed again via convolution with a Bartlett window.

To speed up computation in large datasets WobblyStitcher implements the option to perform the alignment and placement only on a subset or sub-grid of z-planes and fill in the skipped slices via interpolation.

Stitching

In this final step the tiles are combined into a single image. Stitching is done in each z-slice separately by using the optimized positions of the individual tile slices and their shapes to determine the various regions of overlaps together with the tile slices contributing to each of those regions. In addition, for each pixel in each tile slice the distance to the border of that tile slice is determined and passed as a weight for each overlap region to the actual stitching function. WobblyStitcher implements a set of stitching functions, such as maximum, minimum or mean projections as well as interpolations using the pixel weights. Also custom defined stitching functions can be passed. For the vasculature we use a weighted mean using the distance to the border as a weight.

ClearMap 2.0 toolbox

ClearMap 2.0 is designed for advanced and fast image processing of large (Terabyte) 3D datasets obtained from tissue clearing. It is a complete redesign of ClearMap (Renier et al., 2016). The modular source management allows a unified handling of various data sources (image files, binary files, memory maps, shared memory arrays, numpy arrays, GPU arrays, graph formats) and fast parallel 3D image and graph processing as well as interactive visualization of large 3d images.

In the following we provide a brief summary of the ClearMap 2.0 functionality. ClearMap 2.0 is open source software and fully documented. It is available for download under https://github.com/ChristophKirst/ClearMap2.

Alignment methods

- 3d resampling
- 3d alignment to reference atlases (via interface to elastix) (Klein et al., 2010)
- wobbly stitching (see above)
- Allen Brain Atlas annotation modules

Image processing methods

- clipping and normalization
- binary filling
- discrete topology based binary smoothing
- 3d local gradients and Hessian matrices
- 3d tube filter and tubeness measures
- 3d rank filter library (> 30 filters)
- skeletonization via parallel thinning
- 3d tracing
- fast calculation of 3d local image statistics
- equalization methods
- hysteresis and seeded thresholding
- 3d adaptive and local image statistics based thresholding
- light-sheet artifact removal
- fast pseudo deconvolution
- deep convolutional neuronal network based 3d image processing
- expert processing pipelines for specific applications

Graph analysis

- graph preprocessing and cleanup
- graph branch reduction
- graph annotation
- graphs embedded in 3d space
- 3d graphs with 3d edge geometry
- 3d edge geometry post-processing, interpolation, and mesh generation
- morphological operations on edges and vertices
- sub-graph extraction and spatial slicing
- network analysis

On top ClearMap provides a set of visualization tools to visualize large 3d TB datasets and by using overlays or synchronized window displays enables direct inspection of the image processing results.

Visualization tools for 3d images

- fast interactive 2d slice plotting of 3d TB datasets
- overlays and/or synchronized window display of multiple datasets.
- interactive image processing pipeline generation and parameter exploration GUI
- 3d volume rendering
- 3d list and line plots

Visualization tools for 3d graphs

- 3d line plots of 3d graphs
- 3d mesh plots of 3d vasculature graphs with edge geometries

Local histogram statistics and 3d rank filter

Many image processing methods rely on the local histogram or rank order of the voxel intensities in a region around a center voxel under consideration. Calculating those histograms for each voxel is computationally expensive and will strongly slow down the processing in images of terabyte size. ClearMap 2.0 thus provides two optimized ways of calculating those local statistics: (i) a rank filter toolbox using sliding windows to calculate histograms and (ii) histogram sub-sampling and interpolation routines.

TubeMap pipeline

To construct graphs form the vasculature network we designed the processing pipeline TubeMap in ClearMap 2.0 detailed in the following.

Overview: a pseudo-deconvolution step removes shadowing artifacts of large vessels (Figure 2D); an adaptive thresholding captures signal inhomogeneities between and within large filled vessels; an equalization step homogenizes signal gradients across the sample and boosts weaker vessels and capillaries (Figure 2E); a modified tube filter amplifies smaller sized capillary structures with low signal to noise ratio (Figure 2F)

Clipping, masking and first binarization (step 1)

In a first step of the processing pipeline the stitched raw volumetric image is clipped above intensities that can be unambiguously assigned to foreground pixels. Because of 'stray' or 'blur' artifacts from bright vessels (Figure 2D) this upper intensity is chosen conservatively and will only include very large and bright vessels. The voxels clipped in this way contribute the first foreground voxels to the final binary image.

Voxels outside the brain sample show a distinct lower intensity value than even background voxels within the brain. Thus, in parallel to the clipping of high intensities, low intensities are clipped below the sample background and the clipped pixels are designated as background. Non-background pixels are used to define a mask for the brain sample which is used throughout the processing pipeline to restrict all calculations to the brain sample voxels.

Light-sheet artifact correction (step 2)

Light-sheet microscopy introduced 'stripe' and 'shadow' artifacts (Figure 2C). While methods exist to correct for those artifacts (e.g., via Fourier analysis, or stripe detection), they have a high computational demand making them difficult to apply to images of TB size.

We thus developed a method for fast and efficient light-sheet artifact correction. The method uses the fact that the stripe artifact occurs along a predefined axis in the images as the light-sheet always enters the sample from the same direction, and we used a single fixed light sheet illumination. Moreover, background voxels typically show similar intensities along the stripe axis over a certain length scale.

Thus, for each voxel i we estimate the light-sheet stripe artifact intensity I_i by calculating a predefined percentile p_I of the voxel intensities in a region centered around i and highly elongated along the stripe-artifact axis (Figure 2C). The length of this region (or structuring element) for the percentile filter along the stripe artifact axis is chosen to be of the scale on which the stripe artifact intensity changes, while the width and depth are chosen to be below the size of the stripe artifacts cross-section. Subtracting this estimate from the image leads to good corrections of the stripe artifact except at voxels that are part of longer vessels aligned with the artifact axis. To prevent this type of voxels to be removed, we also estimate the local background intensity b_i as the percentile p_b of the voxel intensities in a square shaped region centered around i. The size of this region is chosen larger than the largest vessel structures in the brain sample. This background estimate is compared to the light-sheet artifact estimate and voxel intensity v_i corrected according

$$v_i \rightarrow v_i - \min(v_i, \min(I_i, fb_i))$$

where f is a factor allowing to adjust the background estimate. The result of this correction is shown in Figure 2C.

Processing speed is limited by the local percentile filters. We use our fast 3d rank filter library to speed up the computation. On top, the elongated shape of structuring element for the light-sheet estimate allows further optimization by shifting the structuring elements for local histograms estimation in the direction of the artifact axis. For background estimation we use large structural elements which allow the use of sub-sampling and interpolation.

Median filter (step 3)

In the third step the light sheet corrected image is 3d median filtered with a small structuring element to smooth voxel intensities but preserve edges. We use our fast sliding histogram 3d rank filter library for this step.

Pseudo deconvolution and second binarization (step 4a)

The data showed 'blur' or 'stray' artifacts producing 'halos' of high intensity voxels around bright and large vessels (Figure 2D). Without correction of these artifacts, high thresholds had the tendency to remove weaker and smaller vessels and capillaries connecting to the larger ones, while low threshold values have the tendency to join larger neighboring vessels, even when local or adaptive thresholding was used. While this artifact could be corrected via an appropriate deconvolution step, such a step would add a large computational overhead for our very large datasets.

We thus designed a 'pseudo deconvolution' step that corrects for the 'blur artifact' with much less computational demands. High intensity voxels are identified via a threshold and 'blured' using a 3d Gaussian filter. The blurred result is then subtracted from the original image and the image rectified while the values of the high intensity voxels are preserved (*cf.* Figure 2D).

The resulting 'deconvolved' image is then thresholded at a lower intensity level than the one used to determine the high intensity voxels in order to capture the structure of the bright vessels and the resulting binary added to the final binarized image.

Adaptive threshold and third binarization (step 5a)

In order to capture smaller and less bright vessels the deconvolved image is further subjected to a local histogram-based adaptive threshold and the result added to the final binarized image.

We use our local histogram sampling framework to locally apply the Ridler-Calvard method (Ridler and Calvard, 1978) that determines a threshold by separating the voxels of the image into two groups such that the threshold is midway between the mean intensities of these groups.

Equalization and fourth binarization (step 4b)

While the previous stream of processing and binarization steps (4a,5a) is designed to mainly capture larger or brighter vessels, in parallel we designed a second stream (4b, 5b) for the binarization of weaker and smaller vessels and capillaries. While our clearing and staining protocol is highly optimized to homogeneously label the vasculature, regional variations in the overall luminance exists and particularly smaller and weaker vessels in the deeper regions are often not detected by the first stream of binarizations.

In this step we thus apply a custom designed equalization filter to the median filtered image form step 3. The filter calculates for each voxel i a lower and upper intensity (l_i and u_i) via a lower and upper percentile (p_l and p_u) of the voxel intensities in a rectangular region R_i centered around i. The region is chosen to be larger than the large vessel structures and our efficient histogram sampling framework is used to speed up computation. The voxel intensity is then normalized via

$$v_i \rightarrow f_i v_i$$

with normalization factor

$$f_i = \begin{cases} v_i/l_i & u_i/l_i \leq m \\ m/u_i & \text{else} \end{cases}$$

and m a maximal intensity value for the upper percentile. As a result the image shows a more homogeneous intensity distribution across the sample (Figure 2E).

A fixed conservative threshold is applied to the normalized image and added to the final binary.

Tube filtering and fifth binarization (step 5b)

In a final step, a generalized Frangi tube filter (Frangi et al., 1998; Sato et al., 1998) to enhance smaller vessels and capillaries is applied. The filter first smoothes the image with a 3d Gaussian of a given scale and then calculates the sorted eigenvalues $\lambda_{1,i} \geq \lambda_{2,i} \geq \lambda_{3,i}$ of the Hessian matrix at each voxel i. The tubeness measure t_i is then calculated according to

$$t_i = \begin{cases} |\lambda_{3,i}| \left|\frac{\lambda_{2,i}}{\lambda_{3,i}}\right|^{\gamma_{23}} \left(1 + \frac{\lambda_{1,i}}{|\lambda_{2,i}|}\right)^{\gamma_{12}} & \lambda_{1,i} \leq 0, \lambda_{3,i} \leq \lambda_{2,i} < 0 \\ |\lambda_{3,i}| \left|\frac{\lambda_{2,i}}{\lambda_{3,i}}\right|^{\gamma_{23}} \left(1 - \alpha \frac{\lambda_{1,i}}{|\lambda_{2,i}|}\right)^{\gamma_{12}} & \alpha \frac{\lambda_{1,i}}{|\lambda_{2,i}|} < 1, \lambda_{3,i} \leq \lambda_{2,i} < 0 \\ 0 & \text{else} \end{cases} \quad (1)$$

with parameters $\gamma_{12} = 0.5, \gamma_{23} = 0.5$ and $\alpha = 0.25$ chosen to enhance tube like vessels but also account for their bending (Sato et al., 1998).

A threshold is applied to the tube filtered image to contribute the last part to the final binary image.

Binary filling

In this step, the combined binary image is subjected to a 3d binary filling operation. While the final image is binary and thus already smaller in size it is still a large array. Splitting the filling operation into subsets of the data would entail complex joining operations. TubeMap thus implements a parallel binary filling code based on flood filling from the border that operates on memory maps, allowing the binary filling of arbitrarily sized images not limited by memory.

Deep vessel filling

As antibodies only target vessels walls receptor proteins, larger vessels appear as empty tubes. Given that our method to extract the centerline that relies on topology-preserving 3D thinning, it is necessary to generate solid tubes on the binary mask. Therefore, we designed a method to detect and fill empty tubes to allow a correct centerline extraction via erosion. Vessel filling is a complex task on our data, as the shape, size and continuity of the vessel walls are variable. For this reason, we decided to use a deep convolutional neural network to solve this task.

Architecture

We based the initial network architecture on the DeepVesselNet architecture from Tetteh et al. (2018), which detects the centerline from 3D scans of filled vessels. We iterated modification of this architecture to obtain the following: 2 maxpooling layers followed by 2 3D convolutional layers with dropout with kernel size 7 and 5 and 16 and 32 channels respectively. Then we added a depthwise separable convolutional layer of size 32 with kernel size of 3. Next, two new other convolutional layer are added followed by upsampling layers to get back to the initial input data size before the maxpool layers, and a last convolutional layer of size 2 followed by a center shifted sigmoid function to map output values between 0 and 1, and a softmax layer (Figure S5E).

The depthwise separable convolutional layer (desep conv) consists in a depthwise convolution followed by pointwise convolution. The idea is to increase the network performance while keeping the same amount of parameters.

Optimization function

Our loss function was composed of a classic binary cross entropy Loss to minimize the difference between the output and the ground truth fed to the network:

$$L = -\mathrm{BCE} + \mathrm{CBL}$$

$$\mathrm{BCE} = \frac{1}{N}\sum_{i=1}^{N} y_i \log(\hat{y}_i + (1 - y_i)\log(1 - \hat{y}_i)$$

where N is the number of samples and of a class balancing loss based on Tetteh et al. (2018):

$$\mathrm{CBL} = \mathcal{L}_1 + \mathcal{L}_2$$

$$\mathcal{L}_1 = -\frac{1}{|Y_+|}\sum_{j \in Y_+} \log\left(P(y_i = 1)|X;W) - \frac{1}{|Y_-|}\sum_{j \in Y_-} \log(P(y_i = 0)\,|\,X;W\right)$$

$$\mathcal{L}_2 = -\frac{\gamma_1}{|Y_+|}\sum_{j \in Y_{f+}} \log\left(P(y_j = 0)\,|\,X;W\right) - \frac{\gamma_2}{|Y_-|}\sum_{j \in Y_{f-}} \log\left(P(y_j = 1)\,|\,X;W\right)$$

$$\gamma_1 = 0.5 + \frac{1}{|Y_{f+}|}\sum_{j \in Y_{f+}} |P(y_j = 0\,|\,X;W) - 0.5\,|$$

$$\gamma_2 = 0.5 + \frac{1}{|Y_{f-}|}\sum_{j \in Y_{f-}} |P(y_i = 1\,|\,X;W) - 0.5\,|$$

where Y_+, Y_-, Y_{f+}, Y_{f-} respectively represent the set of positive, negative, false positive and false negative labels.

Vessels account for a minority of voxels (about 15% of the data in our case). This makes the training memory and time consuming as large amounts of data are needed to reach convergence. Therefore, we used a loss which favorizes false positives and strongly penalizes false negative during the training, preventing the network to favor segmenting pixels as background.

Training

To generate a training vascular brain graph for training, we generated datasets comprised only of filled tubes. To obtain such datasets, we designed a preparation of whole head fixation, in order to retain the blood in the tissue (Figure S5A), and see the section "blood retention" for the preparation of these brains. After dissection, we immunostained the brain for circulating immunoglobulins (Liebmann et al., 2016), and complemented it with an immunostaining against podocalyxin to insure a better continuity of the labeled capillaries (Figure S5B), and we double-stained for Smooth Muscle Actin as before. We cleared and imaged the labeled brains with identical conditions to the endothelial wall-stained samples. Vascular graphs were generated using the same multi-path binarization pipeline (Figure 2A) and centerline extraction as all other datasets (Figure S5C). These graphs contain a natural distribution of vessel diameters, which we used to build training cubes of hollow tubes, for which the ground truth is the filled version (Figure S5D). We designed and trained the DNN on these data to fill hollow tubes into solid tubes.

We trained our network on 100*100*100 pixel wide blocks of artificially generated hollow vessels data. From the skeleton, we generated circular empty tubes as input training data and the filled counterpart as ground truth. To diversify the data, we also generated cubes from both the IgG/Podocalyxin dense capillary channel and from the Acta2 channel alone which has sparse arterial tubes. To diversify the vessel radii, we filtered out capillaries (which are already filled at this resolution) from the graph data to only keep vertices corresponding to vessels with larger radii. We also artificially increased the vessel radii on the sparse arterial graph to mimic underrepresented large vessels as they only account for a minority of the vessels in the dataset.

A preprocessing step was added, consisting in adding noise by setting randomly voxel values as foreground to mimic background dots that appears occasionally on binarized data, and train the network to ignore them.

We used a batch size of 8 and trained for 100 epochs.

Application to the vasculature data

We used the network on the CD31 + Podocalyxin stained binarized scans (hollow vessels). The binary masks of 1 channel from 1 hemisphere represents approximately 100Gb and cannot be loaded to the network directly. Therefore we divided the binary masks of the generic vessels (Pdclx + CD31) channel in blocks of 500*500*500 voxel with a 100 voxel overlap in every direction.

We also filled the binary masks of the arterial channel. As Acta2+ vessels have larger radii and are sparse, we used blocs of 900*900*900 voxels with a 200 voxel overlap, and down sampled the blocks by a factor of 4.

Binary smoothing

In the final step we smooth the binary data, as rough surfaces of vessels can lead to artifacts downstream in the skeletonization of the vasculature network. We therefore developed a discrete topology based binary smoothing algorithm based on Németh et al. (2010).

For each voxel *i*the local discrete topology in a 3x3x3 cube C_i centered around *i* is considered and depending on the configuration the center voxel is updated as follows:

If the center voxel is foreground the center voxel is set to background if (i) there are less than three foreground voxels in the cube, (ii) the local topology matches the configuration C_1 or any of its rotations toward each of the 6 faces of the cube (iii) the topology matches C_2 or C_3 or any of the 4 rotations around the z-axis or any of those further rotated toward each face (i.e., 24 rotations), (iv) if the topology matches C_4 or any of its 12 rotations that rotate a fixed edge onto another one (v) the topology matches C_5 or any of its 8 rotations that rotate a corner onto another one.

If the center voxel is background the center voxel is set to foreground if either (i) the number of background pixels in the cube is less than 6, (ii) the inverse topology in which foreground is exchanged with background fulfills either of the conditions for the foreground pixel smoothing above, (iii) the center voxel has at least 3 neighbors in its 6-connected neighborhood and two of those voxels lie along one of the main axes.

The processing of the smoothing is optimized via assigning a unique topological index τ to each possible topological configuration of the 3x3x3 cube around the center voxel and pre-calculating a lookup-table from this index to the resulting center voxel value according to the smoothing rules above. The index τ for each voxel in the image is obtained by considering the binary cube configuration as a 27 bit representation of that index, i.e., by convolving the local cube with a kernel K. To further speed up the computation, we make use of the fact that the kernel K is separable and convolution with it can be calculated via three subsequent one-dimensional convolutions along the three axes.

Skeletonization and graph construction

In a final step of the TubeMap image processing pipeline the binarized image is converted to a graph. The graph construction is done in three steps: (i) the binary image is skeletonized, (ii) loose ends in the skeleton are detected and possible continuations to other loose ends detected via tracing in the non-binarized image data, (iii) the final skeleton is converted into a graph.

Skeletonization

In the first step of the graph construction the binary image is skeletonized. While a large number of skeletonization algorithms exist, they were not suitable for the size of our datasets with running times of over 7 days on our workstation. We thus implemented a fast skeletonization algorithm for terabyte volumetric images that runs in 45min. As skeletonization via thinning is context dependent the processing cannot be easily split into blocks of data. Instead, our algorithm is designed to handle TB sized data as whole. To increase the processing speed, we pre-calculate the thinning actions for all possible local topological configurations into a look-up table and use linear indexing of the image arrays. The algorithm uses 3d parallel thinning with 12 sub-iterations as described in (Palágyi and Kuba, 1999) with a series of optimizations. In short, for each voxel *i* the algorithm decides if that voxel can be thinned away by considering the topology in the local 3x3x3 cube C_i centered on *i* and using the rules defined in (Palágyi and Kuba, 1999) (T1-T14). This process is done in parallel. As parallel thinning of surface voxels may lead to the disconnection of center lines or other topological changes in the final skeleton, the thinning is done in 12 sub-iterations 'attacking' the surface pixels from 12 different directions corresponding to the mid-points of the 12 edges of a cube.

To speed up processing on large images we implemented a series of additional optimizations. First, as the thinning is operating on foreground pixels only and their number significantly decays during the thinning iterations, calculation of the local topological configuration around each voxel is restricted to the foreground pixels only. In each thinning step only voxels that are 6-connected to the background are candidates for removal, so the calculation is further restricted to those border voxels. Second, the topological characterization around each voxel is done using topological indexing together with a pre-calculated look-up table that encodes the thinning rules as described above in the binary smoothing step. Third, all calculations are done on linear arrays using linear indexing, instead of 3d volumetric images. This speeds up addressing foreground pixels and reduces memory requirements by a factor of three. Fourth, all calculations, including candidate voxel detection and topological indexing are parallelized.

The skeleton is post-processed by removing foreground voxels of center lines with at least one endpoint (a foreground voxel with only one neighbor in the 27-neighborhood) and a length to a branch point (a foreground voxel with more than two neighbors) or another endpoint below a critical length. End-points and branch-points detection is efficiently done in parallel by calculating the number of neighbors via convolution with a 3x3x3 cube of ones around each foreground pixel.

End-point tracing

In this optional step, the skeleton is further post-processed by trying to connect loose ends of the skeleton center-lines using tracing in the non-binarized tube-filtered image. To achieve this, the endpoints of the center-lines are detected as described above. For each endpoint an A*-search in the voxel space is performed to find a path with the lowest cost toward the closest endpoint. The cost C for a path $\mathcal{P}$ is defined as

$$C = \sum_{(i,j)\in\mathcal{P}} \frac{d(i,j)}{t_j}$$

where (i,j) is a pair of neighboring voxels (27-neighborhood) in the path, $d(i,j)$ the Euclidian distance between the voxels, and t_i is the tubeness measure defined in (1). If the cost for the path is below a threshold the path is added to the binary image. If the cost is too high, a path to the binary mask of the vasculature is traced using the same cost function. If the cost is below a threshold the path is added to the binary mask. The resulting binary is re-skeletonized as described in the previous step.

The purpose of this tracing step is to detect small vessels of weak intensity that were partly missed in the binarization process and thereby to reduce the number of open ends in the vasculature graph. For our datasets and with the above described equalization methods this step was usually not necessary (*cf.* Figure 2).

Graph construction

To facilitate the analysis of the vasculature network, the skeletonized binary image is turned into a graph representation that captures the topology of the vasculature network. A graph $G = \{V, E\}$ is a collection of vertices $v_i \in V$ and edges $e_{i,j} \in E$ between two vertices v_i and v_j. The vasculature network carries additional geometric information (e.g., vessel shape or radius) and can be accompanied by additional local data (e.g., expression levels of molecular markers). We thus consider graphs in which the vertices and edges hold a set of additional properties $(p_k(v_i), p_l(e_{i,j}))$, such as spatial, geometric or molecular information.

Graphs extracted from the vasculature consist of millions to hundreds of millions of vertices. To enable the analysis of those large graphs, TubeMap provides a high-performance graph module based on the graph-tool library (Peixoto, 2014) and boost graph libraries https://www.boost.org/doc/libs/1_66_0/libs/graph/doc/index.html). In addition to a large number of graph manipulation and analysis routines, our module also provides graph classes that handle the spatial geometry and other annotational information, as well as the visualization of the graphs in 3d space.

In TubeMap, graph construction from the skeletonized image is done as follows: first, a raw graph is constructed by turning each foreground voxel of the skeleton into a vertex that also carries the positional information of the voxel. The vertices are then connected via undirected edges if they are neighbors (27-neighborhood) in the skeleton image. This process can result in local all-to-all connected cliques with more than 2 vertices at branch points of the skeleton. Thus, those cliques are identified and replaced by a single vertex with a coordinate position that is the mean of the clique vertices. Isolated vertices or small components not connected to the giant component are typically removed from the graph for downstream analysis.

In a second step, the raw graph is reduced to a branch graph consisting of vertices that are endpoints or branch-points only (i.e., vertices v_i with edge degree $d(v_i) \neq 2$). The vertices of this graph are then connected by edges if there is a path of vertices of degree 2 between them. The connection is done via tracing in the raw graph. In this process, the positional, geometric and other information attached to the vertices along a path between two branch-vertices is collected and attached as a property to the new edge connecting the two branch-points.

Vasculature graph geometry extraction

To capture the geometry of the vasculature network, TubeMap, besides storing the positional information about the center lines of the vessels also detects their shape. In particular, the radius of the vessel at each vertex or each point in a branch is estimated by taking the pre-processed equalized image and measuring the distance to the nearest voxel in which the intensity decayed by half. To avoid measuring radii within hollow tubes, the nearest voxel search is started outside the final binarized image in which hollow tubes are filled.

Vasculature vertex and branch labeling

TubeMap enables measuring the expression of other markers obtained via multi-color stainings and imagining along the vasculature graph. A set of tools is provided to measure those, including methods to measure the histogram, mean, maximum or minimum expression levels within a structural element centered on each voxel of the extracted graph or within a region described by the local extracted vessel geometry.

To measure the expression of the smooth muscle marker Acta2, we measure maximum expression levels around each point of the vasculature graph within a spherical region with a radius equal to the estimated radius of the vessel at that point. Branches are labeled positive for Acta2 if the majority of points in that branch have expression levels above a certain threshold.

TubeMap provides further routines to post-process edge and vertex labels based on geometric or other measures and label continuity. In particular, binary labels can be subjected to morphological operations acting on the graph topology. This includes binary morphological closing that can be used to fill gaps in a sequence of branch labels. In addition, labels of vertices or edges can also be traced along the graph topology according to arbitrary passed rules that act on the geometry or other vertex or edge properties, providing a generalized hysteresis thresholding operation for a given labeling. For the vasculature graph we use a one-step morphological closing as well as tracing based on the radial measure to post-process the Acta2 branch label. Reconstruction of

the vasculature network was corrupted by dense vessel crossings as well as preparation artifacts on the brains cortical surface. Thus, to avoid errors in the artery and vein labeling the tracing of arteries and veins was stopped when the distance to the surface fall below a certain threshold. The distance of each branch to the brain surface in turn was calculated by an Euclidian distance transform from the background into the brain using the 3d brain atlas annotation image.

Vasculature graph atlas annotation

TubeMap provides functions to annotate data with labels from reference atlases, such as the Allen Brain Atlas. Annotation is done by acquiring an additional reference image in parallel to the other data channels and align this to the corresponding reference image of the atlas. We used an autofluorescence template from the ABA at 25μm generated from serial 2-photon tomography. To achieve the alignment, TubeMap first resamples the auto-fluorescent image of the sample to the resolution of the atlas reference and then aligns the image in 3d non-linearly. TubeMap integrates the elastix package functionality (Klein et al., 2010) for the non-linear alignment. For the vasculature data a hierarchical estimation of b-spline transformations between the two reference images is used together with a cross-entropy measure to quantify the local alignment quality. For the vasculature data, the reference image is acquired in tiles directly after each tile of the other channels and thus the same alignment and stitching layout can be used to assemble the full reference image. To correct for small misalignments between reference and data images a rigid transformation between both is estimated using also a cross-entropy measure. The resulting joint transformation from data to sample reference to atlas reference is used to transform the coordinates of the graph points onto the reference frame of the atlas. In the final step, the transformed positions of the graph are used to extract the atlas annotation and any other atlas information.

The TubeMap graph module implements routines to extract statistics, sub-graphs or other information based on these annotations. The atlas annotation can also be used for 3d rendering of the vasculature graph.

QUANTIFICATION AND STATISTICAL ANALYSIS

Statistical analysis

All statistics were conducted with the Scipy Python library (https://scipy.org). Throughout the manuscript, data are represented as means with standard deviation. For comparisons of the means between two groups, non-parametric Mann-Whitney test were used (Figures 6E, 7A, 7B, 7D, and 7I). All sample sizes, precision measures and p values are indicated in the figure legends. In all instances, n represents the number of mice used. Further details on specific quantifications are given in the following sections.

Branch point density, branch density, branch length and tortuosity

Branch point density and branch density were defined as the number of branch points or branches per volume in each brain region, respectively. The volume of each brain region was estimated by summing the volume of all voxels belonging to that region using the reference atlas annotation.

The length of each branch was measured as the sum of the Euclidean distances between consecutive pairs of coordinates that define the branch as extracted from the raw graph.

Branch tortuosity was defined as the ratio between the length of the branch divided by the Euclidean distance between its endpoints.

Shortest paths to arteries and veins

Shortest paths from all branch points in the brain to the arteries and veins were computed via a graph-topology based distance transform algorithm. The graph-topology based distance transform was implemented in TubeMap via iteratively propagating artery or vein labels on the graph topology and at the same time keeping track of the iteration number at each propagation step (i.e., the shortest distance to the newly reached branch points). To consider the different lengths of each branch, the distance transform was computed on the raw graph instead of branch graph in which each branch is expanded to a chain of vertices corresponding to the branch length. While this introduces a small error when compared to the actual Euclidian lengths of the branches, it allows computing the shortest distances of all branch points at once, significantly speeding up the calculation and enabling a brain wide analysis. As a result, each branch point is assigned a distance to the closest artery branch as well as the closest vein branch. In a final step, only the distances at each original (non-expanded) branch point are kept. The shortest path length from arteries to veins running through a specified branch point was then calculated as the sum of those distances at the branch point under consideration.

Arterial domains

The capillary vasculature network is highly recurrent and redundant making it in principle difficult to identify domains that are 'fed' by a single arterial vessel. However, this analysis aimed at identifying those vasculature domains supported by arterial vessels based on shortest distances. In order to do so, we first identified isolated arterial vessels by labeling connected components in the arterial network (only the branches identified as arteries). To separate penetrating arteries into the cortex, the arterial network on the brain surface was removed before detecting the components. Each component was then given a unique label and all labels were iteratively propagated in parallel to the unlabeled capillary network. As a result, each capillary was assigned to its closest arterial component, defining the arterial domains.

Distances of vasculature graph features between cortical regions

The goal of this analysis was to analyze differences in the vascular organization and its layered structure between cortical regions. In order to do so, we used the ABA annotation to extract a set of features of the vasculature graph for each layer of each cortical region and compared those. Wee extracted the following five features: number of branching points (all vessels), number of arterial branching points, number of arterial end points, number of radially oriented vessels, and number of planar oriented vessels. The number of radially and planar oriented vessels was determined by first calculating the normalized orientation vector of the vessel. A vessel was counted planar (radial) oriented if the length of the orientation vector projected onto the planar plane (onto the radial axis) was larger than 0.7.

To finally compare cortical regions, we first normalized each feature resulting in a distribution of each feature across the 6 cortical layers. We then calculated the earth-movers distance (or ''Wasserstein distance'') between those distributions to obtain the overall distance between each pair of cortical layers. The earth-movers distance can be understood via the following picture: let each distribution be represented by a pile of sand. The distance between those distributions then simply is the work or cost to move the least amount of sand to transform one pile to another. Thus, the more the shapes of the distributions differ, the costlier it is to transform them, and the larger the distance between them.

Finally, after having obtained the distance matrix between all cortical regions, Ward clustering was performed to identify groups of cortical regions sharing similar distances to other regions.

Stochastic block model analysis

While the arterial domain analysis above was targeted at identifying sub-regions defined by arterial supply, in this analysis we aimed at identifying sub-networks or modules in the vasculature network based on the graph-topology alone. In order to do so we used an inference-based approach.

More precisely, we assumed that the adjacency matrix of the vasculature graph G is captured by a stochastic block matrix composed of B blocks with a number n_s of nodes in each block s and a number e_{sr} of random edges between blocks s and r with $s, r \in \{1, \ldots, B\}$ (Holland et al., 1983). Probabilistic inference is then done on this model given the observed vasculature graph using the implementation described in (Peixoto, 2014). In short, as edges are assumed to be random between blocks, all graphs with the block structure $C = (\{n_s\}, \{e_{sr}\})$ are equally probable. Thus the likelihood of observing a graph G that already has the block structure C is $P(G \mid C) = \Omega(C)^{-1}$ where $\Omega(C)$ is the total number of different graphs with block structure C. For a fixed block number B this likelihood can be maximized using a Markov Chain Monte Carlo algorithm that iteratively changes block memberships of individual nodes (Peixoto, 2014). In order to find the optimal block number B a minimum description length criterion is used to compare the different models (Peixoto, 2014, 2017).

DATA AND CODE AVAILABILITY

Example datasets, links for ClearMap, ClearMap 2.0 and TubeMap codes download, tutorials and bench protocols are available online at https://idisco.info. Data are available on OSF: https://osf.io/sa3x8/?view_only=4427a838cbd0468c9fbad9cab465d866. The codes are also accessible from GitHub at https://github.com/ChristophKirst.

Supplemental Figures

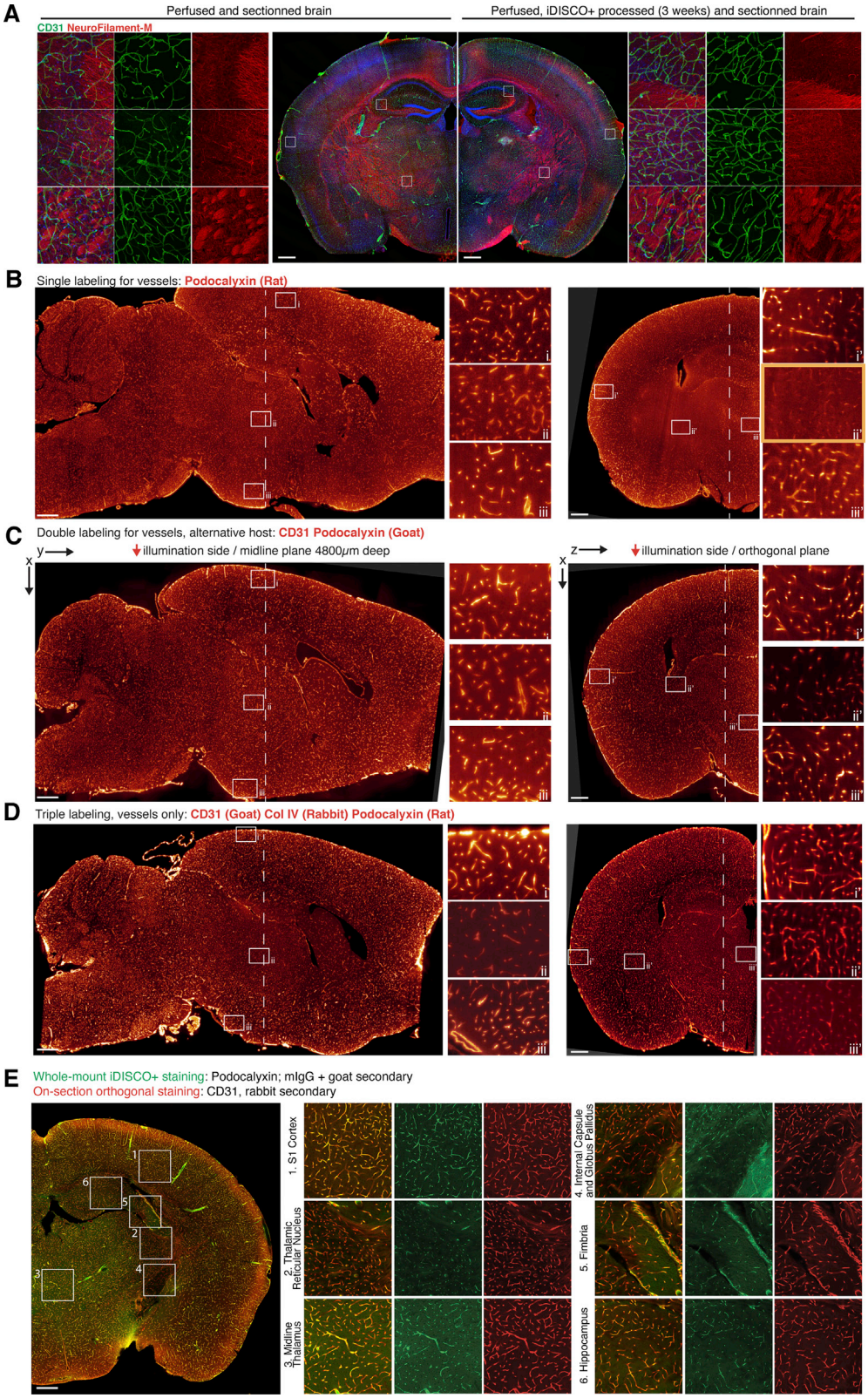

(legend on next page)

Figure S1. Deep Immunolabeling of the Vasculature, Related to Figure 1

(A) Comparison of the tissue and vascular integrities after iDISCO+ processing: coronal 100μm sections of perfused brains (left) or iDISCO+ processed brains (right), immunostained for Neurofilment M and CD31. The iDISCO+ processing of the tissue doesn't visibly affect the vascular or axonal morphology compared to classic immunohistochemistry at this imaging scale. B-E Hemispheres triple immunolabeled with iDISCO+, light sheet scanned and tiled at 4X. A plane is shown close to the midline, as well as an orthogonal reconstructed plane (dotted lines). Insets detail the signal taken at different extremities of the 3D volume, close (i or i') or away (iii or iii') from the imaging and illumination sides. (B) Alternative single labeling of the vessels using rat anti-Podocalyxin only. While this strategy offers the maximal flexibility for counter stains, the signal in the lateral thalamus is very low, but still segmentable (highlighted inset). (C) Alternative double labeling of the vessels against CD31 and Podocalyxin with goat-raised antibodies (D) Alternative triple immunolabeling for the vessels (CD31, Collagen IV and Podocalyxin) further improves the labeling gradient over the dual labeling (CD31, Podocalyxin) and has the best signal to noise ratio, while being less flexible for counter stainings. (E) Validation of the whole-mount passive immunolabeling. Brains whole-mount immunolabeled with the iDISCO+ protocol with primary (Podocalyxin) and secondary rounds of staining, then vibratome sliced and re-stained for CD31 on sections (n = 3). A thalamic section (the most challenging region of the brain in whole-mount stainings), is shown with several insets of different representative regions. Whole-mount and on-section immunolabels overlap perfectly in all regions inspected, surface, deep, as well as in gray and white matter. A rare exception is highlighted: a few capillaries were not detectable in the whole mount staining in the white matter of the cingulate cortex, as shown in E5. Scale bars are 500μm.

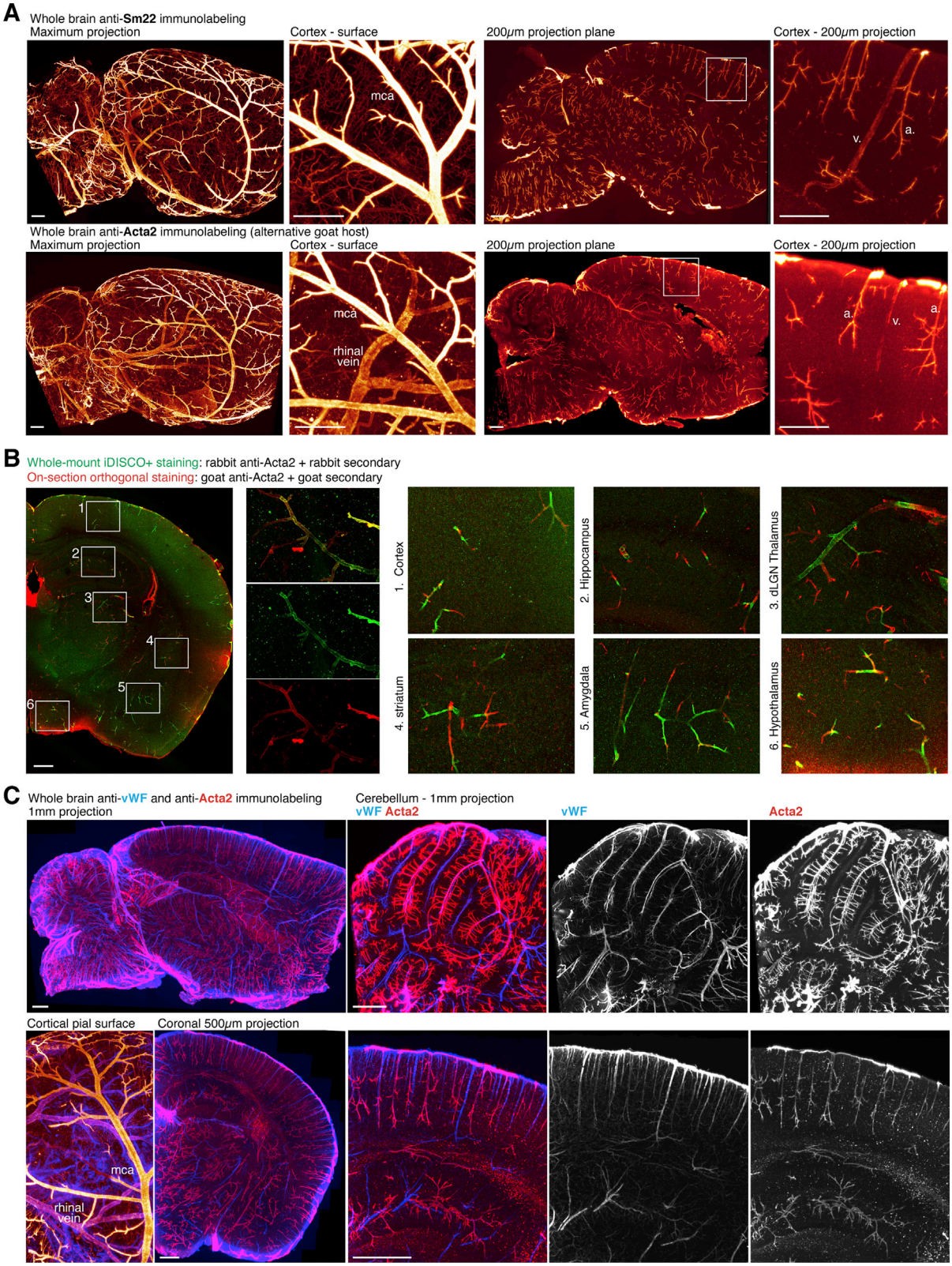

(legend on next page)

Figure S2. Deep Immunolabeling of Arteries and Veins, Related to Figure 1

(A) Whole brain immunolabeled with iDISCO+ for markers enriched in arteries: sm22 (upper panels) and acta2 (lower panel, alternative host, goat). Lateral projections as well as a 200μm central plane projection are shown. Both markers show comparable staining patterns in the arteries. Expression of both sm22 and acta2 is visible only in a few very large veins. Acta2 expression is also high in the rhinal vein at the cortical surface, while it is sm22 negative. Large veins in general have a patchier distribution and weaker signal than arteries for both markers, which is used as a criteria for later annotations. (B) Overlay of the whole-mount immunolabeling for acta2 (in green, rabbit) with an orthogonal acta2 staining on sections (in red, goat). Both antibodies are raised against the same epitope. A coronal section at the thalamic level is shown. While all arteries are double-labeled, arterioles (low diameter acta2+ vessels) are occasionally only visible from the section staining (arrows, and examples shown in insets). (C) Whole brain iDISCO+ labeled for acta2 and Von Willebrand Factor (vWF). Coronal and sagittal 1mm deep projections are shown. vWF expression is enriched in veins throughout the brain, while also detectable at weaker levels in arteries. The quasi-exclusive presence of veins in the white matter of cerebellar lobules is visible in midline projections. Scale bars are 500μm.

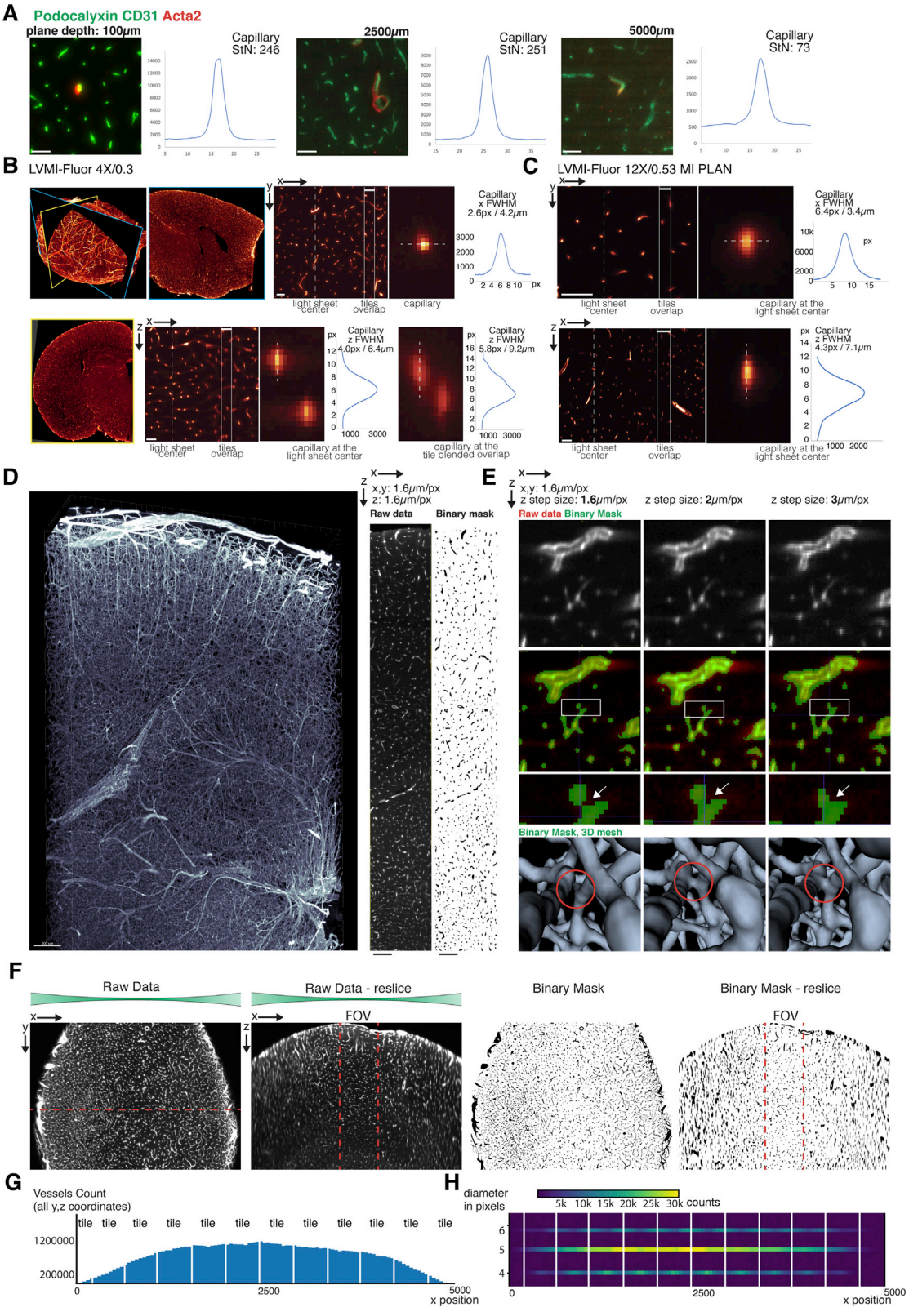

(legend on next page)

Figure S3. Maximization of the Imaging Resolution, Related to Figure 1

(A) Evaluation of the signal to noise ratios of capillaries at several depth in a iDISCO+ whole-brain prepared with a triple immunolabeling (CD31, Podocalyxin, Acta2) and scanned at the center of the sample with light sheet microscopy. The images show a constant StN ratio between the surface and the center of the scan at 2500μm. Only at the center of the sample, at 5mm, the scattering starts to be noticeable with a StN ratio of 73. (B) Whole brain stained for Podocalyxin and CD31 imaged with the LaVision LVMI-Fluor 4X/0.3 objective at high light sheet numerical aperture (0.14). Detail of the cross-section of a capillary shown in x,y and x,z reslices, with the corresponding intensity profiles. Depending on its position at the center or on the edge of a tile, the apparent diameter of a capillary will vary between 4 and 6 pixels in the axial direction, but is stable at 3 pixels in the lateral directions. (C) Imaging whole brains with the 12X/0.53 objective generates an apparent diameter of 6 pixels in the lateral directions, closer to the real capillary size, but doesn't improve the axial resolution, which stays unchanged compared with the 4X objective. D-E Tests of the step size to maximize the resolution of the image processing. (D) A tile extracted from a whole brain scan. The maximal intensity projection of the tile, an x,z resliced plane and its binary mask are shown. (E) Detail of the resliced data acquired at different step sizes. Raw resliced data, their binary masks and a mesh projection of the mask are shown. At 2 and 3μm, the resolution is adequate for capillaries, but would fuse the masks of nearby object (red circle). While slightly oversampled for the axial optical resolution, a 1.6μm step-size allows the disambiguation of the masks of some fused vessels. (F) Effect of the light sheet profile on the vascular binary mask. Whole-brain immunolabeling for CD31 and Podocalyxin, iDISCO+ cleared and imaged at a light sheet NA of 0.14. The raw data are presented in the left panel, and the mask on the right side. For each, the original acquisition plane is shown with the (x,z) reslice, highlighting the loss of resolution due to the light sheet heterogeneity along the x-axis. A possible field of view (FOV) crop, between which the binary mask appears isotropic, is suggested (red dotted lines). (G) Effect of the tiling strategy on the number of detected capillaries and their sizes. The tile edges do not introduce a detectable loss of capillary segmented (upper histogram). (H) The diameter distribution along the x-axis shows that most capillaries are measured at a diameter of 5 pixels. The rest of the measured capillary diameters are labeled at 4 or 6 pixels. The detected radii frequency is spatially influenced by the position of the capillary on the tile with a 2 pixels amplitude. As a conclusion, all capillary diameters are measured between 4 and 6 pixels. Scale bars are 50μm (A,B,C)

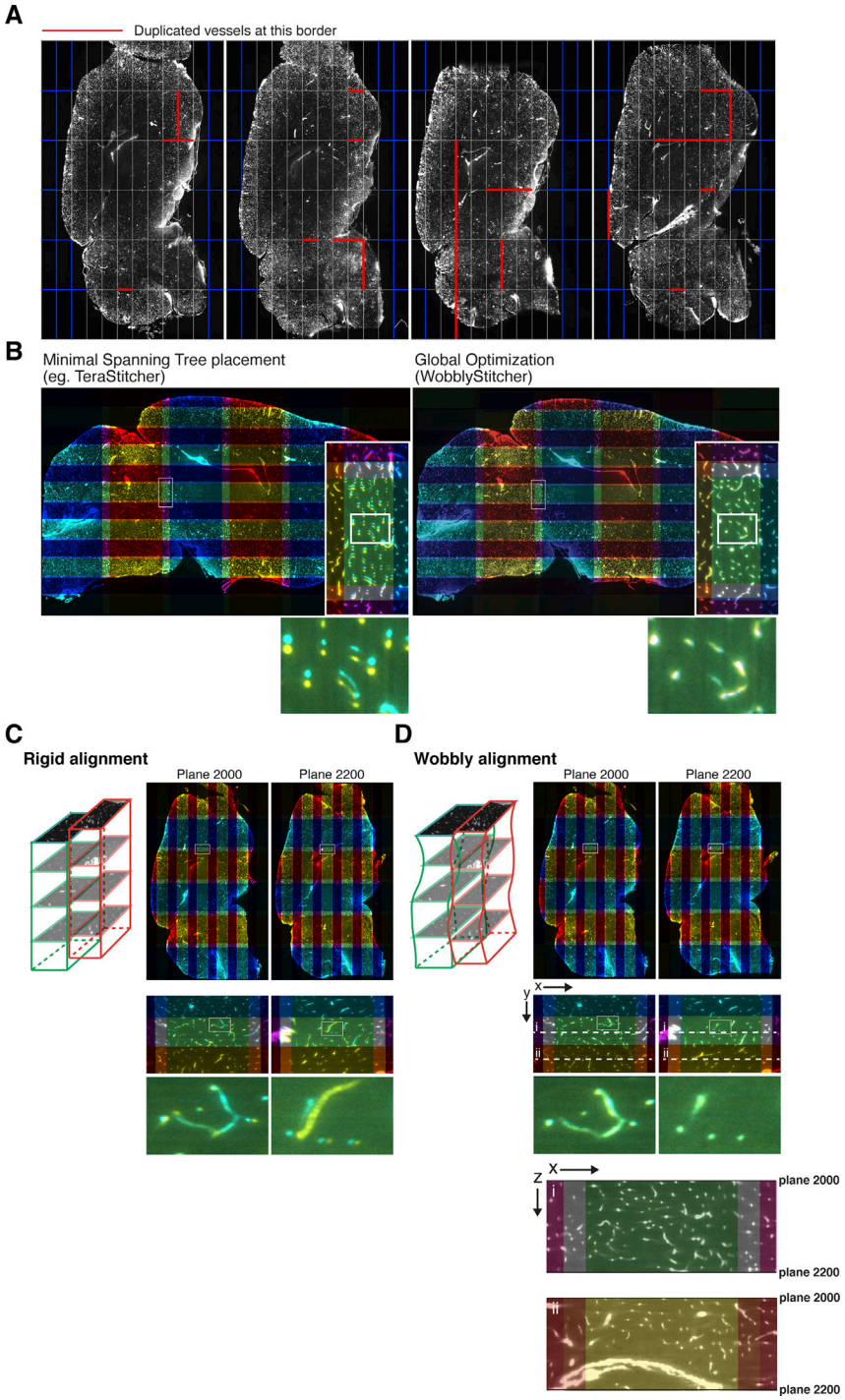

Figure S4. Correction of Common Tiling Artifacts in Large Datasets, Related to Figure 1

(A) 4 brains, immunolabeled with the blood retention protocol, where aligned using TeraStitcher. The red edges indicate a duplication of the vessels in the blended tile overlap after alignment. (B) Correction of the tiles misplacement with Global Optimization. C-D Two planes shown at z = 2000 and 2200 (plane numbers) of the same brain rigidly aligned without correction (C) or with the wobbly correction (D). While the placement by global optimization improves the vessel continuity, duplications are still visible in select planes: the vessels shown in the inset are correctly placed in the plane 2000, but not in 2200. The wobbly alignment (non rigid x,y displacement of the planes along the z-axis) corrects the misalignments on both planes. (x,z) reslices are shown inside the tile and at the level of the blended overlap to highlight the consistency of the data after the wobbly alignment.

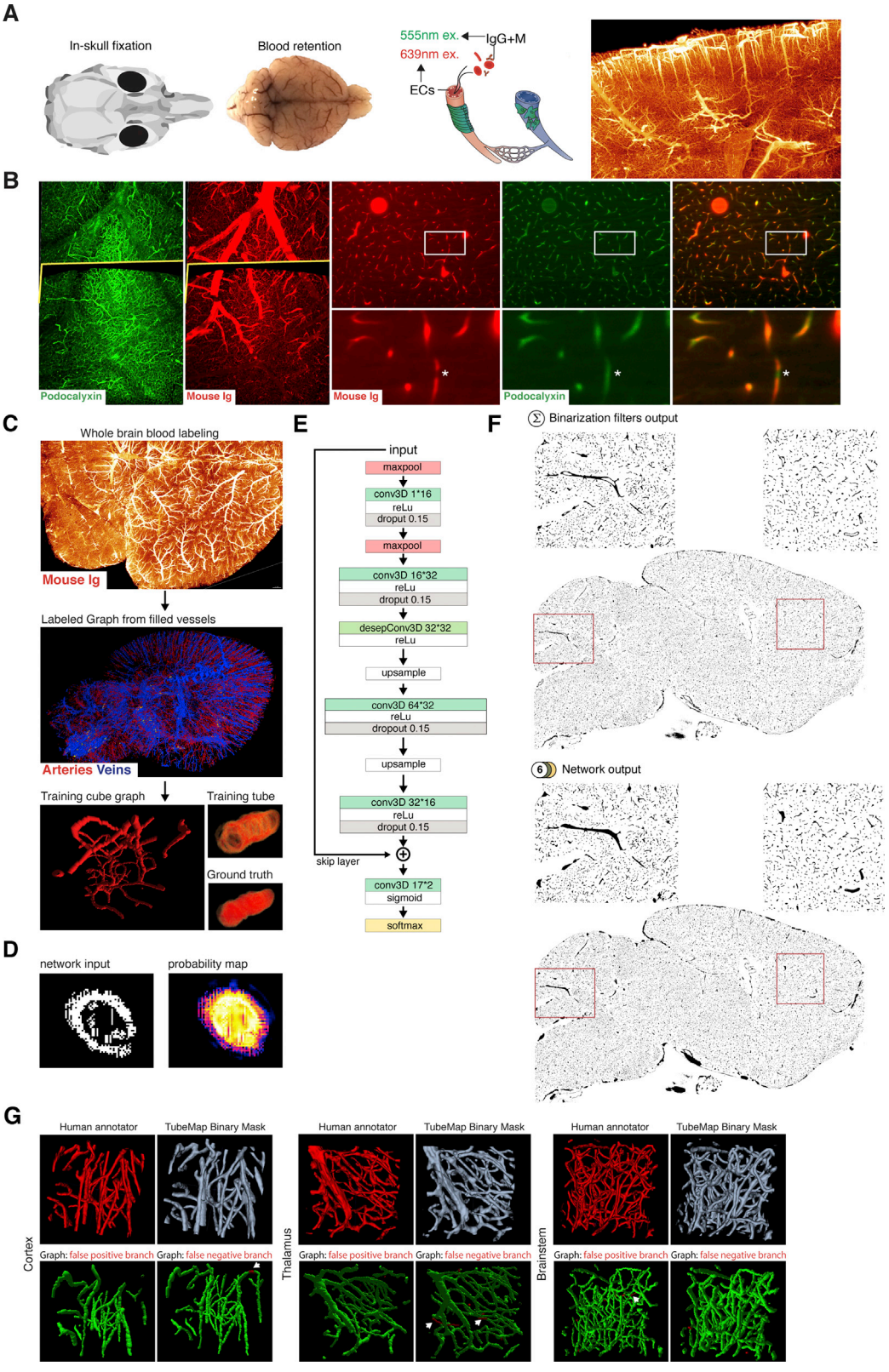

(legend on next page)

Figure S5. Hollow Tube Filling via a Deep Convolutional Network, Related to Figure 2

(A) A strategy to generate filled datasets to train the Deep Neural Network: mice are sacrificed unperfused to retain the blood in the vasculature, the skin is removed and the animal immersed in fixative. The brain is dissected after 4 days (middle panel). The blood is clearly visible in the surface veins. The serum is labeled against circulating IgGs, and combined with a podocalyxin co-labeling. (B) Typical results of the whole-blood immunolabeling. Maximum projection through a tile from a whole brain scan. A section plane is indicated in yellow, and details of this plane shown in the center and right panels. The mouse IgG labeling enables the visualization of filled vessels (barely visible in the Podocalyxin labeling, green). The star shows an example of vessel discontinuity in the IgG labeling, corrected from the Podocalyxin labeling. (C) Generation of datasets and model cubes to train a tube-filling neural network: brains are dissected with their vessels still filled with serum through blood retention, iDISCO+ processed and imaged with the same conditions as the regular datasets. The centerlines of the filled vessels from whole brain scans are extracted and used to generate training cubes of artificial hollow vessels, with sizes and densities matching the normal distribution in the brain. (D) Filling of a tube generated from the brain graph (detail from the test cube), and probability map of the added foreground (E) Architecture of the vessel filling DNN. (F) Output of the multipath filter pipeline. A single plane close to the center of the brain is shown. The insets show a caudal region (cerebellum) and rostral (cortex) containing several empty tubes. (G) Output of the tube filling network. The output is based on both the vessel channel and the acta2 channel. Of note, very big veins outside the brain are often missed by the filling, as they do not appear as acta2 positive vessels (an exemple is visible at the ventral surface, close to the circle of Willis). Arteries and smaller veins are efficiently filled by the network. (G) Blocks of raw data annotated by a human annotator (mesh projection of the annotation shown in red). The TubeMap binarization is shown in blue and was performed on the full brain from which the cubes are extracted. Graph are generated from both masks (human and TubeMap), and then the graph branches are compared to the binary mask. Arrows indicate disagreement between the human annotator and TubeMap.

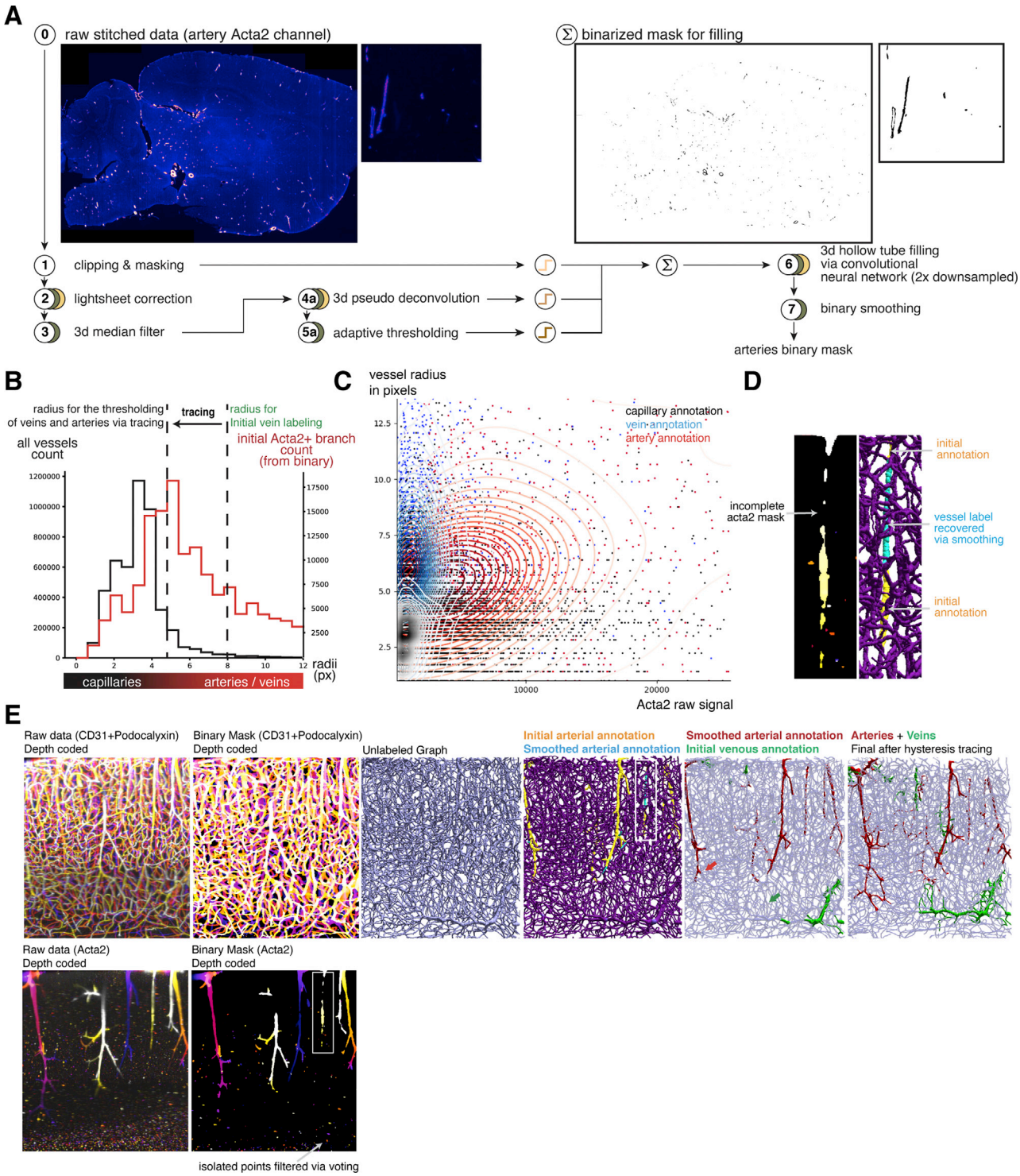

Figure S6. Automated Annotation of Veins and Artery, Related to Figure 3

(A) Binarization pipeline for the arterial imaging channel (acta2). This binarization pipeline is modeled from the full vasculature binarization (Figure 2A), but adapted to the sparse nature of arterial datasets. (B) Distribution of vessel radii for all vessels (black) or Acta2+ vessels (red). The initial seed points for veins and arteries tracing are placed on large vessels, which are rare in the dataset, and the vessel label is then traced down to smaller radii. (C) Joint distribution of vessel radii and Acta2 signal levels after tracing. Traced veins and arteries are indicated in blue and red respectively (D) Smoothing of the vessel labels can help recover

(legend continued on next page)

interrupted initial annotations from the Acta2 binary mask (E) Example of the labeling pipeline on a cube of data extracted from a whole brain scan. Raw data are color-coded by depth for clarity. The unlabeled graph is generated from the binary vessel mask. Arterial edges on the full graph are labeled based on their co-localization with the arterial binary mask. Gaps in the initial labeling are then removed by a smoothing operation along the graph edges. Vein label seeds are then added to the large acta2- vessels (initial venous annotation). Smaller arterioles and venules are finally labeled by tracing down the initial annotations to smaller radii.

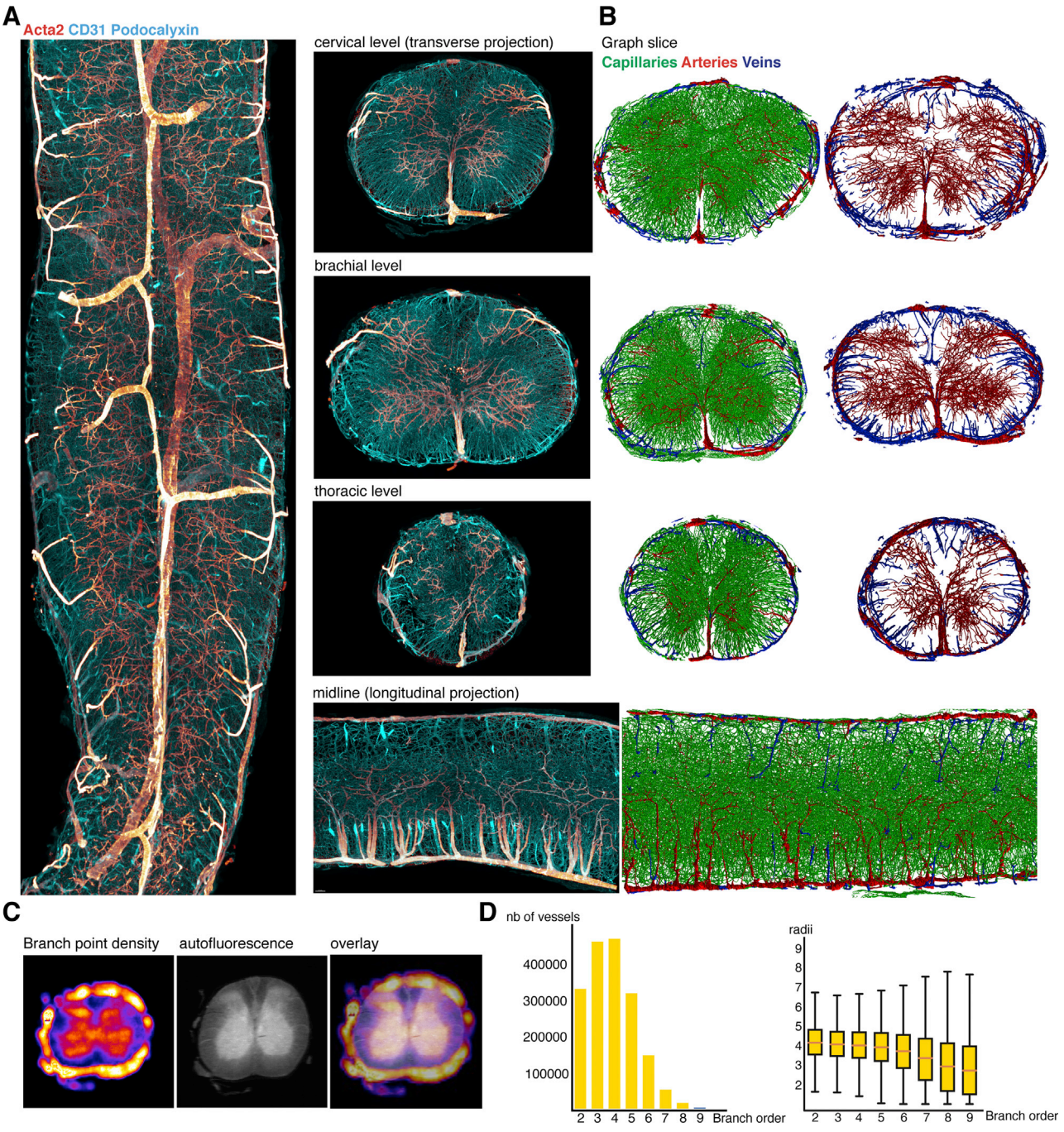

Figure S7. Reconstruction of the Spinal Cord Vascular Network, Related to Figure 4

A-B Upper segments of the spinal cord (cervical to upper thoracic levels), labeled for CD31, Podocalyxin (blue) and acta2 (red). The anterior spinal artery is strongly positive for acta2, while the posterior spinal vein is also visible with a weaker acta2 signal. Collateralizations of the posterior spinal arteries are visible on each sides. Coronal projections of the reconstructed graphs highlight the arterial domains from the anterior spinal artery in the ventral horn and the posterior spinal arteries in the dorsal horns. Ingressions from the anterior and posterior veins are also annotated and visible in the midline projections. (C) Heatmap of the branch point density, example of a brachial level: higher densities of branch points are visible in the gray matter and pial surface compared to the white matter (D) Diffusion from arteries in the upper spinal cord. The left panel shows the distribution of the number of vessels across arterial distances (given as branch order from the closest artery). Most vessels are within 2 to 5 branches from the closest artery. This distribution is similar than the one calculated in the brain. The right panel shows the distribution of radii for each step away from an artery, which is also similar than in the brain, and shows larger radii (from venous components) from order 6 through 8.